

## Characterization of multilayer rough surfaces by use of surface-plasmon spectroscopy

E. Fontana\* and R. H. Pantell

*Electrical Engineering Department, Stanford University, Stanford, California 94305*

(Received 11 December 1986; revised manuscript received 26 June 1987)

Earlier attempts to characterize rough surfaces by means of surface-plasmon spectroscopy have been unsuccessful [H. Raether, *Surf. Sci.* **125**, 624 (1983)]. In the present paper we show that certain assumptions in the theoretical model were inappropriate. Correcting these assumptions we are able to obtain excellent agreement between predicted and experimental intensities of both specular and diffuse scattering from a rough surface.

### I. INTRODUCTION

In recent years, increasing attention has been focused on the search for simple techniques capable of probing the properties of surfaces. Particular emphasis has been given to the use of optical methods for *in situ* and non-destructive observation of the structure of interfaces and thin films.

From a comparison of reflectivities of coated and uncoated substrates, as in reflection spectroscopy,<sup>1</sup> one can obtain information about the thickness and optical parameters of the film. However, since this technique is based on a discrimination between reflectivities, the determination of very thin coating thicknesses in the angstrom dimension scale can only be achieved with the use of highly sophisticated differential reflectance techniques.<sup>1</sup>

Another approach that has been used extensively is ellipsometry,<sup>2</sup> which measures the changes introduced in the polarization of light undergoing reflection from a coated substrate. In this way, quantitative information on the optical constants or thickness of the coating can be obtained, and the technique is sensitive enough to measure thicknesses down to angstrom dimensions.<sup>2</sup> Theoretical and experimental studies have also demonstrated that ellipsometry can be combined with other techniques, e.g., reflection spectroscopy, for the characterization of surface roughness.<sup>3</sup>

Although high precision can be achieved with the use of this technique, the operation of a null ellipsometer usually requires a large number of manipulations to control the combination of optical elements that sets the polarization of the incident light to provide a linearly polarized reflection.<sup>1,2</sup> Electronically controlled ellipsometers, as already in commercial use, overcome these difficulties, but these instruments can become rather costly for certain applications.

A very simple optical technique that can accurately characterize the structure and optical parameters of surfaces and thin films is surface-plasmon spectroscopy (SPS). It is based on measurements of dispersion and damping of surface plasmons (SP's),<sup>4</sup> which are electromagnetic modes that can propagate along the interface between two media, one of which has a negative dielectric constant. For the visible and infrared portions

of the spectrum, metals and some semiconductors<sup>5</sup> exhibit a negative permittivity and can support the existence of these surface modes. The electromagnetic fields associated with the SP are evanescent along the direction normal to the interface within both media. The fact that the energy of the wave is localized at the boundary makes SP's particularly sensitive to changes either in the geometry or the dielectric properties of the interface.

The basic principle underlying SPS is shown in Fig. 1. A plane-polarized laser beam is incident through a prism having a metal coating of a few hundred angstroms on its base. The coupling prism is not required to be hemicylindrical as indicated in Fig. 1, and in principle, any triangular shaped prism can be used. For incidence angles greater than the total internal reflection value for the prism-to-vacuum interface, a SP can be excited between the metal and vacuum. Further increase in the incidence angle leads to a drop in the reflected intensity. The minimum of this intensity occurs at a particular incidence angle for which the phase velocity of the incoming beam parallel to the prism base matches the SP phase velocity. The width and depth of the reflected intensity

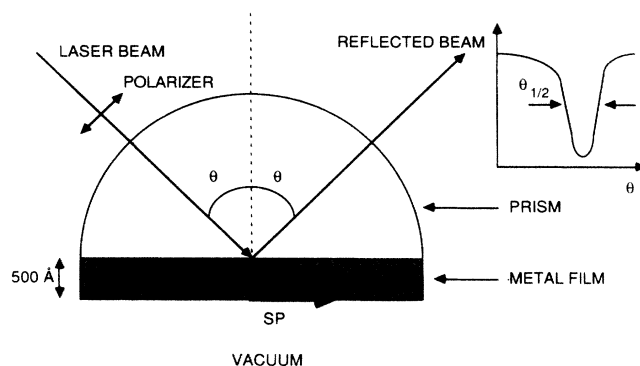


FIG. 1. Experimental configuration illustrating the excitation of a surface plasmon (SP) (Ref. 6). For incidence angles  $\theta$  above the total internal reflection value, an evanescent wave exists into the vacuum region. A resonant drop in the reflectivity is observed as the angle  $\theta$  is increased above this value. The minimum in the curve occurs when the phase velocity component of the incoming beam parallel to the prism-metal interface plane matches the SP phase velocity in the metal-vacuum interface.

as a function of angle measures the damping and strength of the excitation, respectively. Typically, these reflectivity curves, as shown in the inset of Fig. 1, and as referred to in the literature as attenuated-total-reflection (ATR) curves, can have a very sharp resonance. (e.g.,  $\frac{1}{2}^\circ$  full width at half maximum, for a silver film 500 Å thick at  $\lambda = 5461$  Å.<sup>6</sup>) This provides an accurate way to simultaneously determine the thickness and complex permittivity of the metal film under study.<sup>7-9</sup> In addition, the existence of small disturbances close to the metal surface can significantly alter the shape and position of the ATR curve. Measurable changes can be observed, for example, by the presence of a dielectric coating as thin as 1 Å,<sup>7</sup> or by the existence of roughness of similar size on the surface of the metal film.<sup>10-13</sup>

Probably the most important feature that serves to distinguish SPS from the optical techniques described previously is its simplicity. In contrast to reflection spectroscopy, high accuracy is achieved without the use of any sophisticated detecting electronics, for the measured intensity itself is sensitive to perturbations near the metal surface. In contrast to ellipsometry, SPS requires a small number of optical elements for its implementation and basically the control of a single variable; namely, the incidence angle illustrated in Fig. 1. In addition, an intensity measurement is much simpler than the experimental determination of light polarization, as in ellipsometry. Furthermore, the ATR curve depicted in Fig. 1 yields three parameters at a single wavelength<sup>4</sup> (e.g., film thickness and a complex permittivity), one more than the number of parameters that can be measured using either reflection spectroscopy or ellipsometry under the same conditions.

One should notice that SPS is not limited to the analysis of metal films or coatings on the surface of these films. Any multilayer system can be characterized by placing it in close proximity to the metal-vacuum interface in the prism configuration of Fig. 1.

A variety of applications for surface plasmons has been proposed and demonstrated. Pockrand *et al.*<sup>7</sup> demonstrated the usefulness of the technique for measurements of thickness and optical constants of organic monolayers. Their results showed excellent agreement with those obtained by other methods. Flanagan and Pantell<sup>14</sup> used the SPS technique to obtain fast determination of antibody concentration in biological systems and suggested the use of this approach for the design of optical immunosensors. Surface plasmons have also been used in the design of polarizing structures in optical planar waveguides.<sup>15</sup> Due to the high-field concentration associated with SP's, they have been used to enhance nonlinear surface phenomena<sup>16</sup> and have played a role in the field-enhanced Raman effect of adsorbates on metal surfaces.<sup>17</sup>

The potential for applications, added to the simplicity of the SPS technique, has motivated the investigation reported in the following sections. In this paper, we are concerned with the applicability of SPS to the characterization of rough surfaces. Although this field has received considerable attention recently,<sup>10-13,18,19</sup> the effect of roughness on SP properties has not been properly described, leading to large discrepancies between theory

and experiment.<sup>19</sup> It is the aim of this paper to discuss the current theoretical models and the approximations associated with these models. We will show that certain assumptions that are part of existing analyses are inappropriate, and we will present a corrected version for SPS that can be used to characterize rough surfaces.

## II. THE EFFECT OF ROUGHNESS ON THE SP RESONANCE

Many of the experiments reported in the literature have been made on silver films with thicknesses ranging from 350 to 700 Å.<sup>10-13</sup> Rough surfaces were obtained by depositing an underlayer of CaF<sub>2</sub>, LiF,<sup>20</sup> or Ag (Ref. 13) onto a smooth quartz substrate prior to silver deposition (Fig. 2). The roughness of CaF<sub>2</sub>, for example, increases with CaF<sub>2</sub> thickness and the average dimensions of the irregularities (parallel to the plane of the surface) are in the (100-1000)-Å range.<sup>20</sup>

To obtain quantitative information about the roughness parameters of silver films with underlayers of CaF<sub>2</sub>, Hornauer<sup>12</sup> measured the scattering and reflection of light with SP excitation. Since this article appears to be one of a few in the literature reporting measurements of both specular and diffuse scattering in the same sample with sufficient information about the experimental parameters needed for a theoretical evaluation, we have chosen to use these data for the analytical calculations of the present paper.

The experimental arrangement for measuring specular reflection<sup>12</sup> makes use of the ATR technique<sup>6</sup> illustrated in Fig. 3. A *p*-polarized laser beam i.e., polarized in the plane of incidence, of intensity  $I_0$  is incident on the metal film through the prism at an angle  $\theta$ . The light wave-vector component parallel to the metal surface is given by<sup>21</sup>

$$k_x = \frac{2\pi}{\lambda} n \sin\theta, \quad (1)$$

where  $n$  is the prism refractive index and  $\lambda$  is the optical wavelength. By increasing the angle  $\theta$  above the critical angle  $\theta_c = \sin^{-1}(1/n)$ , the light beam couples to a SP at the metal-to-air interface. This condition is observed by a resonant absorption in the specularly reflected intensity.<sup>6</sup> The angle  $\theta_{\min}$  for which the specular light intensity is a minimum in the ATR curve determines the SP wave

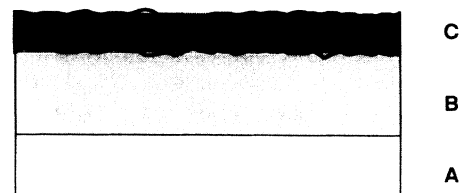


FIG. 2. Roughness simulation with use of underlayer. Region A is a glass substrate, region B is the underlayer (CaF<sub>2</sub>, LiF, MgF<sub>2</sub>, or Ag) which produces the irregularities on the metal surface. The metal is designated as region C.

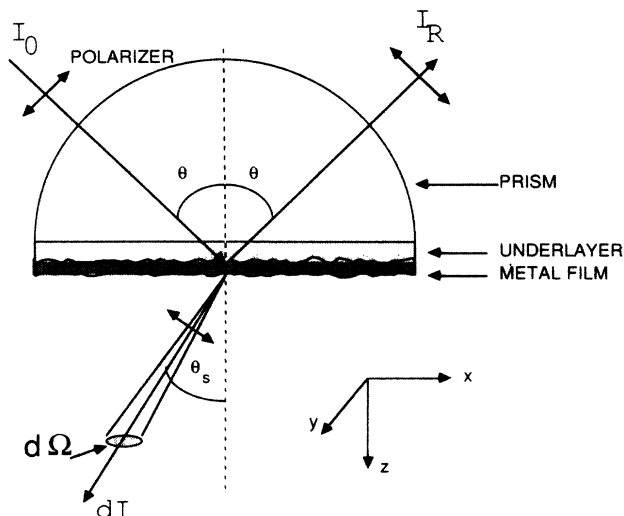


FIG. 3. Experimental arrangement for measuring specular and diffuse scattering intensities from thin metallic films.

vector  $k_{SP}$ . From Eq. (1), we have

$$k_{SP} = \frac{2\pi n}{\lambda} \sin\theta_{\min}. \quad (2)$$

The half-width  $\theta_{1/2}$ , of the resonance curve, gives information about the attenuation of the SP as it propagates.<sup>21</sup>

The scattered diffuse light was measured with the incident light angle fixed at  $\theta_{\min}$ , and a photomultiplier was used to record the angular dependence of  $dI/d\Omega$ , the scattered intensity per unit solid angle. The observation planes for both specular and diffuse scattering in Fig. 3 coincided with the incidence plane. The *s*-polarized scattered intensity was also measured by Hornauer<sup>12</sup> in order to check for the presence of dielectric inhomogeneities in the metal film, a method proposed by Kroger and Kretschmann.<sup>22</sup> It was concluded that surface roughness, rather than dielectric inhomogeneity, was the main mechanism responsible for the scattered intensity.

Optical-quality flat-glass slides were used as substrates for the  $\text{CaF}_2$  underlayers (0, 500, 1000, and 2000 Å thick), all of them with a 500-Å-thick silver film. Each multilayer thus prepared was then brought into optical contact with the prism shown in Fig. 3. Specular and diffuse scattering data could thus be taken and compared for the different configurations. Prism and substrates are made of quartz whose refractive index is within ~1% of the  $\text{CaF}_2$  refractive index. Thus, after optical contact, prism, substrate, and  $\text{CaF}_2$  underlayers can be considered, for all practical purposes, to compose a single optical unit. Two ATR curves obtained at  $\lambda=4500$  Å are displayed in Fig. 4 corresponding to  $\text{CaF}_2$  thicknesses  $d_{\text{CaF}_2}$  of 0 Å (smooth silver film) and 1000 Å. (It should be noted that the data for the rough-surface specular reflection reported in Ref. 12 are represented by the permittivity  $\epsilon_{\text{Ag}}$  and the thickness of the Ag film  $d_{\text{Ag}}$ , which were altered to produce the curve for the rough film using reflection formulas for a smooth film. We used these modified parameters to obtain the rough-film curve shown in Fig. 4.) From Fig. 4 for the rough film one no-

tices the displacement of the ATR curve to higher  $\theta$  values along with an increase in the linewidth.

In Fig. 5, as extracted from Ref. 12, the angular dependence of the normalized *p*-polarized scattered intensity per solid angle element  $dI/I_0 d\Omega$  is shown in polar coordinates for different  $d_{\text{CaF}_2}$ . The *p* polarization means that the electric field is parallel to the observation plane and the latter coincides with the incidence plane. As can be seen from this figure, with increasing  $\text{CaF}_2$  thickness, the angular distribution of scattered intensity becomes broader and the peak position, which is sharply defined in the forward direction for the "smooth" film, turns to the backward direction. In addition, the maximum of scattered intensity increases with increasing  $d_{\text{CaF}_2}$ , indicating a larger roughness for thicker  $\text{CaF}_2$  films. Since, for a perfectly smooth metal surface there should be no diffuse scattered light due to the evanescent nature of the wave extending into the vacuum region shown in Fig. 2, the curve labeled smooth in Fig. 5 indicates that the Ag film having no  $\text{CaF}_2$  underlayer also exhibits some degree of roughness.

Theoretical investigations of the effect of roughness on the propagation characteristic of SP's have been conducted using different approaches. The surface current model developed by Stern<sup>23</sup> and generalized by Kröger and Kretschmann,<sup>22</sup> replaces the rough interface between two media by a smooth one with an equivalent surface current distribution whose strength is, to a first-order approximation, proportional to the surface height variations. Maradudin and Mills<sup>24</sup> analyzed the scattering of light from rough surfaces with a Green's-function technique, which was further extended by Maradudin and Zierau<sup>25</sup> to account for the change in the dispersion relation of SP's due to roughness. Toigo *et al.*<sup>26</sup> approached the question of reflectivity of rough surfaces by solving the boundary problem by means of the Rayleigh-Fano method<sup>27,28</sup> which, when restricted to the small roughness limit, gives results in agreement with the ones obtained by the previous approaches.<sup>29</sup> This agreement indicates that the theory can be used to describe the influence of rough surfaces on SP's. Nevertheless, the model has been applied inappropriately to describe the experimental situation, as the next paragraphs demonstrate.

In the theoretical models for predicting the intensity and angular distribution of diffuse scattering, the rough surface is described statistically. In this context, one needs to assume an autocorrelation function  $h(\rho)$  for the surface, and the one which has been used most extensively in the literature<sup>23-26</sup> is a Gaussian,

$$h(\rho) = \delta^2 \exp(-\rho^2/\sigma^2), \quad (3)$$

where  $\rho$  is the distance between two points on the surface. The parameter  $\sigma$  is the correlation length, which is the distance over which  $h(\rho)$  decreases to  $e^{-1}$  of its maximum value. It gives a measure of the dimension of peaks and valleys measured parallel to the plane of the surface. The symbol  $\delta$  is the root-mean-square deviation of the surface from flatness along a direction normal to the surface. The theoretical expressions for the diffusely scat-

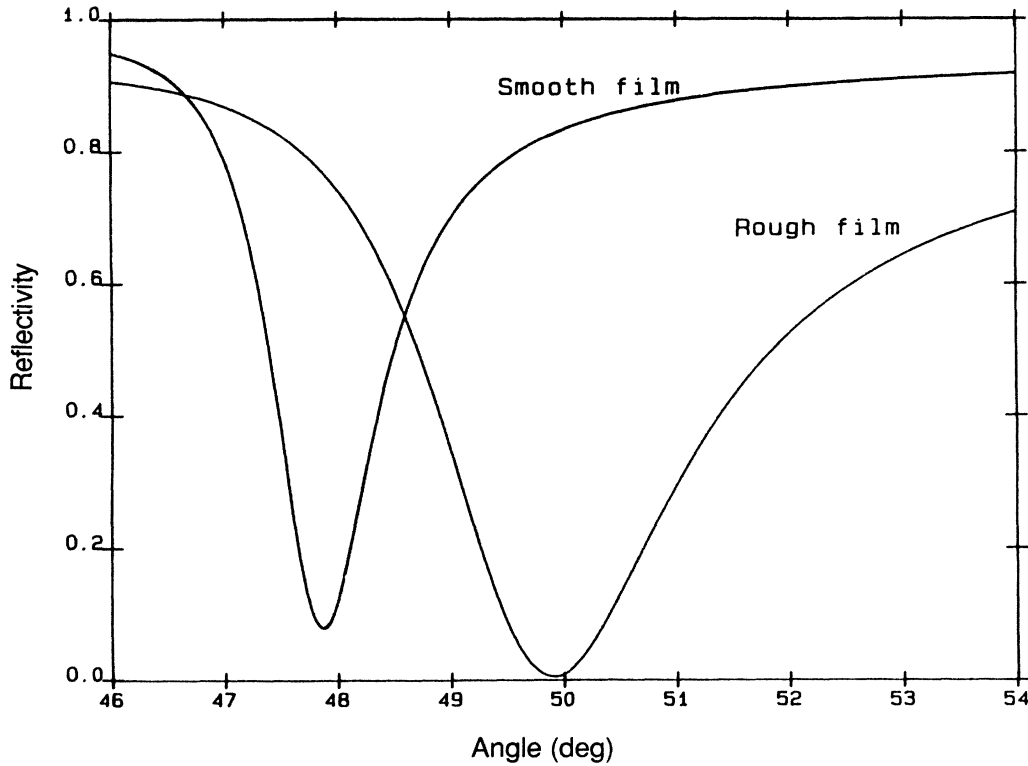


FIG. 4. Attenuated total reflection (ATR) curves obtained in Ref. 12 at  $\lambda=4500 \text{ \AA}$ . The "smooth" curve is for  $d_{\text{Ag}}=500 \text{ \AA}$  and  $\epsilon_{\text{Ag}}=-6.83-i0.26$ . The "rough" curve is for  $d_{\text{CaF}_2}=1000 \text{ \AA}$  and was determined by calculating the reflection from a smooth surface with altered parameter values:  $d=542 \text{ \AA}$  and  $\epsilon_{\text{Ag}}=-5-i0.46$ .

tered intensity as well as for the change in dispersion relation of SP's due to roughness are dependent on the parameters  $\delta$  and  $\sigma$ .<sup>23-26</sup> (Also, see Sec. II.)

Using the theoretical expression for the scattered intensity [See Eq. (A33)] and introducing the modifications in the thickness and dielectric constant of the silver film to account for the change in the ATR curves for the different  $d_{\text{CaF}_2}$ , Hornauer obtained, from the data of Fig. 5, the numbers given in Table I. The correlation length was roughly the same, at  $\sigma=850 \text{ \AA}$ , for all  $d_{\text{CaF}_2}$ . To see how well these numbers represent the data, we have selected the parameters corresponding to  $d_{\text{CaF}_2}=1000 \text{ \AA}$ , i.e.,  $\delta=18 \text{ \AA}$  and  $\sigma=850 \text{ \AA}$ , and calculated the angular dependence of the scattered intensity. This calculated intensity is shown in Fig. 6 together with the experimental data extracted from the polar diagram of Fig. 5. As can be seen from Fig. 6, the model does not provide a very good fit to the data.

The discrepancy becomes even worse if one tries to reproduce the ATR curve shown in Fig. 4 for  $d_{\text{CaF}_2}=1000 \text{ \AA}$ . Following the procedure described by Raether,<sup>19</sup> the details of which are given in Secs. III A and IV, we obtain the results shown in the second column of Table II together with the experimental data from Fig. 4. These are expressed in terms of the change in the resonance angle,

$$\Delta\theta \equiv \theta_{\min}(d_{\text{CaF}_2}(=1000 \text{ \AA})) - \theta_{\min}(d_{\text{CaF}_2}(=0 \text{ \AA}))$$

and the increase in the ATR curve half-width,

$$\Delta\theta_{1/2} \equiv \theta_{1/2}(d_{\text{CaF}_2}(=1000 \text{ \AA})) - \theta_{1/2}(d_{\text{CaF}_2}(=0 \text{ \AA})).$$

The theoretical predictions were based upon the values for  $\delta=18 \text{ \AA}$  and  $\sigma=850 \text{ \AA}$  obtained from the diffuse scattering measurements.

These comparisons between theory and experiment indicate that there is a difference of 1-2 orders of magnitude. In Sec. III we will examine the assumptions used in the theoretical calculations that led to the predictions described in this section. Then, we will present an analytical procedure that will eliminate the discrepancies between theory and experiment.

### III. ANALYSIS

In the analysis proposed in this paper, we will consider only the changes introduced by surface roughness on the specular and diffuse intensities. Material inhomogeneities have been suggested as another possible source for the discrepancies between theory and experiment for measurements of light scattering obtained from quasismooth metal surfaces.<sup>30</sup> Although inhomogeneities could introduce changes in the specular and diffuse intensities, as pointed out previously Hornauer<sup>12</sup> showed that this effect is negligible for the parameters of his experiment. Thus,

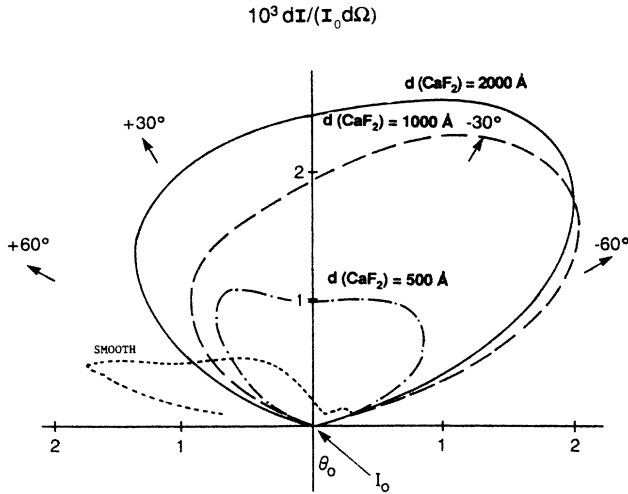


FIG. 5. Polar plots of plane-polarized diffuse scattered intensity obtained in Ref. 12 for different  $\text{CaF}_2$  thicknesses. Curves are for  $d_{\text{CaF}_2} = 500, 1000,$  and  $2000 \text{ \AA}$ , respectively. The dotted curve is the angular distribution of intensities for a smooth silver film. In each case, the incidence angle is set on the corresponding value for SP resonance.

we will not consider material inhomogeneities in the analysis discussed in the next paragraphs.

#### A. Assumptions in the existing theory

The procedure used by Raether<sup>19</sup> to account for the ATR data in Ag films roughened by underlayers of  $\text{CaF}_2$  is based on a number of assumptions. First, the estimates for the shift and broadening of the ATR curves, as reported in Ref. 19, made use of the numerical results obtained by Sari, Cohen, and Scherkoske<sup>18</sup> for the dispersion relation of SP's propagating in a single, rough, silver-air interface. Consequently, it is assumed in Raether's estimates that the thickness of the Ag is infinite, rather than having the finite thickness used in the experiments. While it is true that for a 500- $\text{\AA}$ -thick film the phase velocity of the SP wave is approximately that of an infinitely thick film, the excitation amplitude does depend upon  $d_{\text{Ag}}$ . In turn, this means that the linewidth of the ATR depends upon  $d_{\text{Ag}}$ .

Furthermore, the theoretical evaluation of the roughness effect on the dispersion relation of SP's in the single interface, as calculated by Sari and co-workers, was obtained only in an approximate form. This approximation will be discussed in Sec. IV. In the present analysis, the

TABLE I. Ag film roughness for different  $d_{\text{CaF}_2}$  for  $\sigma = 850 \text{ \AA}$  obtained in Ref. 12.

$d_{\text{CaF}_2} (\text{\AA})$	$\delta (\text{\AA})$
0	4
500	12
1000	18
2000	35

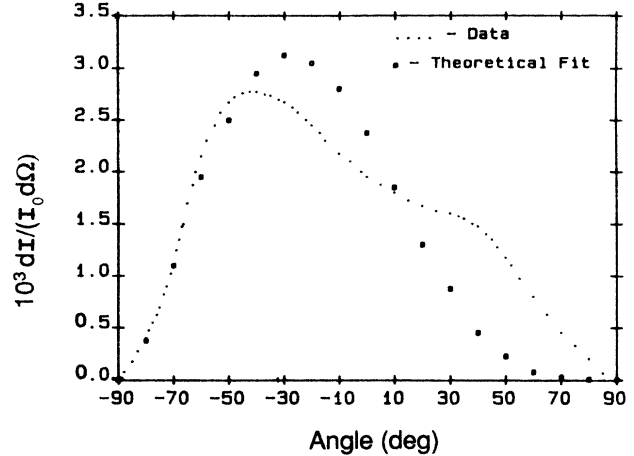


FIG. 6. Angular dependence of diffuse scattered intensity for Ag on an underlayer of  $\text{CaF}_2$  ( $1000 \text{ \AA}$ ). The dotted curve is the data extracted from Ref. 12. Small circles represent the theoretical prediction for  $\delta = 18 \text{ \AA}$ ,  $\sigma = 850 \text{ \AA}$ , and the modified optical parameters given in Ref. 12.

approximation used by Sari and co-workers will be removed. The use of this approximation will be shown to lead to wrong results for the modified dispersion relation of SP's.

Finally, an additional effect which has been neglected in the theoretical model<sup>19</sup> is the roughness of the underlayer onto which the Ag film is deposited. Electron micrographs of  $\text{CaF}_2$  films reveal structures with height variations and bump widths on the order of  $1000 \text{ \AA}$ .<sup>31</sup> The roughness of the underlayer plays a role in the theoretical analysis and, indeed, the inclusion of this effect is essential for explaining, consistently, both the specular and diffuse scattering experiments.

#### B. Theoretical model

To analyze the influence of roughness on the properties of SP's we consider the rough boundary shown in Fig. 7, with the mean height located at the  $z = z_0$  plane. The electromagnetic fields on each side of the boundary at  $z = \xi$  satisfy the conditions

$$\begin{aligned} \mathbf{n} \times \Delta \mathbf{E} &= \mathbf{0}, \\ \mathbf{n} \times \Delta \mathbf{H} &= \mathbf{0}, \end{aligned} \quad (4)$$

where  $\mathbf{n}$  is a vector normal to the interface and can be written as

TABLE II. Specular reflection from a rough silver film. Theory is calculated from Eq. (A42) with  $\lambda = 4500 \text{ \AA}$ ,  $\epsilon_{\text{Ag}} = -6.83 - i0.26$ ,  $\delta = 18 \text{ \AA}$ ,  $\sigma = 850 \text{ \AA}$ .

	Experiment <sup>a</sup>	Sari approximation	Theory [using Eq. (A42)]
$\Delta\theta$ (deg)	2	0.27	0.026
$\Delta\theta_{1/2}$ (deg)	1.75	0.05	0.028

<sup>a</sup>Reference 12.

$$\mathbf{n} = \left( \frac{\partial \xi}{\partial x}, \frac{\partial \xi}{\partial y}, -1 \right) \quad (5)$$

and  $\xi = \xi(x, y)$  describes the surface height variations of the boundary around its average plane. In the above,  $\Delta \mathbf{E}$  and  $\Delta \mathbf{H}$  represent the difference between the electric and magnetic fields, respectively, above and below the rough interface. The fields in (4) are developed as power series in  $\xi$  around  $z = z_0$  in the form

$$\Delta \mathbf{E}(\xi) = \Delta \mathbf{E}(z_0) + \xi \frac{\partial}{\partial z} \Delta \mathbf{E} \Big|_{z_0} + \frac{\xi^2}{2!} \frac{\partial^2}{\partial z^2} \Delta \mathbf{E} \Big|_{z_0} + \dots$$

with a similar expansion for  $\Delta \mathbf{H}$ . It has been shown<sup>22</sup> that, to first order in  $\xi$ , the boundary conditions given by Eq. (4) can be satisfied by incorporating a current source term into Maxwell's equation

$$\nabla \times \mathbf{H} = \mathbf{J} \delta(z - z_0) + \epsilon_0 \frac{\partial \mathbf{E}}{\partial t} \quad (6)$$

with  $\mathbf{J}$  given by

$$\mathbf{J} = \epsilon_0 \left[ (\epsilon_1 - 1) \frac{\partial \mathbf{E}_1}{\partial t} - (\epsilon_2 - 1) \frac{\partial \mathbf{E}_2}{\partial t} \right] \Big|_{z=z_0} \xi(x, y), \quad (7)$$

where  $\epsilon_1$  and  $\epsilon_2$  are the permittivities in regions I and II, respectively, and  $\delta(z - z_0)$  is the Dirac  $\delta$  function. The source term given by Eq. (7) exists in the region  $R$  having the smooth boundaries illustrated in Fig. 7. The other source terms given in the literature,<sup>22</sup> both electric and magnetic, are negligible for wavelengths  $\lambda$  such that the small roughness condition  $(2\pi |\epsilon_1 \text{ or } 2|^{1/2} \xi / \lambda) \ll 1$  is satisfied. This inequality is met reasonably well for the range of parameters considered in this paper.

The use of the equivalent current approach has the advantage of replacing rough surfaces with currents located between smooth surfaces. This allows, with a simple extension of the method, for the analysis of multilayer rough surfaces.

It is convenient to express the fields in terms of their transforms.

$$\begin{aligned} \mathbf{A}(\mathbf{r}, z) &= \int_{-\infty}^{\infty} \int_{-\infty}^{\infty} d\mathbf{k} \mathbf{a}(\mathbf{k}, z) \exp(-i\mathbf{k} \cdot \mathbf{r}), \\ \mathbf{a}(\mathbf{k}, z) &= \frac{1}{(2\pi)^2} \int_{-\infty}^{\infty} \int_{-\infty}^{\infty} d\mathbf{r} \mathbf{A}(\mathbf{r}, z) \exp(i\mathbf{k} \cdot \mathbf{r}), \end{aligned} \quad (8)$$

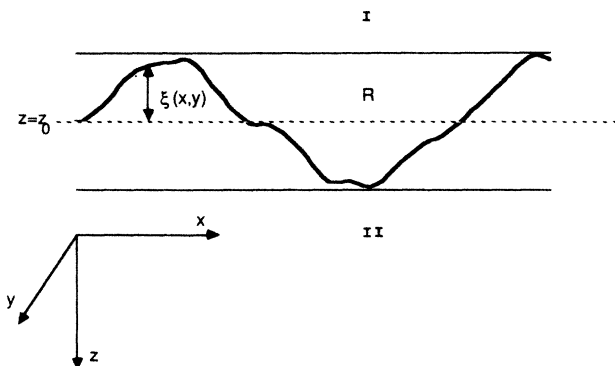


FIG. 7. Definition of the smooth boundaries region ( $R$ ) which encompasses the rough surface.

with  $\mathbf{k} = (k_x, k_y, 0)$ , a two-dimensional wave vector  $\mathbf{r} = (x, y, 0)$ , and an  $e^{i\omega t}$  time dependence is assumed. The integration variables in Eq. (8) are defined by  $d\mathbf{k} \equiv dk_x dk_y$  and  $d\mathbf{r} = dx dy$ . Capitals and small letters on the left-hand side (lhs) of Eq. (8) represent quantities in the coordinate and  $\mathbf{k}$  space, respectively.

We introduce  $p$ - and  $s$ -polarized fields according to the definitions

$$\begin{aligned} \mathbf{e}_p &= e_p(\mathbf{k}, z) \mathbf{k} + e_z(0, 0, 1), \\ \mathbf{h}_p &= h_p(\mathbf{k}, z) k_{\perp}, \\ \mathbf{e}_s &= e_s(\mathbf{k}, z) k_{\perp}, \\ \mathbf{h}_s &= h_s(\mathbf{k}, z) \mathbf{k} + h_z(0, 0, 1), \end{aligned} \quad (9)$$

where  $\mathbf{k}_{\perp} = (-k_y, k_x, 0)$ . The  $p$  waves are polarized in the plane of incidence and the  $s$  waves are normal to this plane.

Relationships between the transformed fields in regions I and II (refer to Fig. 7) are obtained by the following procedure.<sup>22</sup>

(a) The radiation fields in region  $R$  are calculated by solving the inhomogeneous wave equation resulting from the presence of the source term given by Eq. (7).

(b) Equation (4) is applied to the smooth boundaries between regions I and  $R$  and between regions II and  $R$  to relate the fields in regions I and II to the fields in region  $R$ .

This method leads to Eqs. (10)–(13). For  $p$  waves,

$$e_{p1}(\mathbf{k}, z_0) - e_{p2}(\mathbf{k}, z_0) = \frac{1}{\omega \epsilon_0} j_z(\mathbf{k}, z_0), \quad (10)$$

$$h_{p1}(\mathbf{k}, z_0) - h_{p2}(\mathbf{k}, z_0) = -j_p(\mathbf{k}, z_0),$$

with

$$j_p(\mathbf{k}, z_0) \equiv \frac{1}{k^2} [k_x j_x(\mathbf{k}, z_0) + k_y j_y(\mathbf{k}, z_0)]. \quad (11)$$

For  $s$  waves,

$$e_{s1}(\mathbf{k}, z_0) - e_{s2}(\mathbf{k}, z_0) = 0, \quad (12)$$

$$h_{s1}(\mathbf{k}, z_0) - h_{s2}(\mathbf{k}, z_0) = j_s(\mathbf{k}, z_0),$$

with

$$j_s(\mathbf{k}, z_0) \equiv \frac{1}{k^2} [k_x j_y(\mathbf{k}, z_0) - k_y j_x(\mathbf{k}, z_0)]. \quad (13)$$

The subscripts 1 and 2 refer to the fields in regions I and II, respectively.

Now, we apply the above procedure to analyze the multilayer system of Fig. 8, which corresponds to the experimental situation. With reference to the experimental arrangement of Fig. 3, medium I in Fig. 8 represents the prism with refractive index  $n$ ; medium II, the metal (Ag) with dielectric constant  $\epsilon = \epsilon_r + i\epsilon_i$  and thickness  $d$ ; and medium III is a vacuum with  $\epsilon_3 = 1$ . The  $\text{CaF}_2$ -to-Ag roughness is represented by the surface profile  $\xi_1(x, y)$ , and  $\xi_2(x, y)$  defines the Ag-to-vacuum interface. The coordinate system in Fig. 8 is defined such that  $z = 0$  and

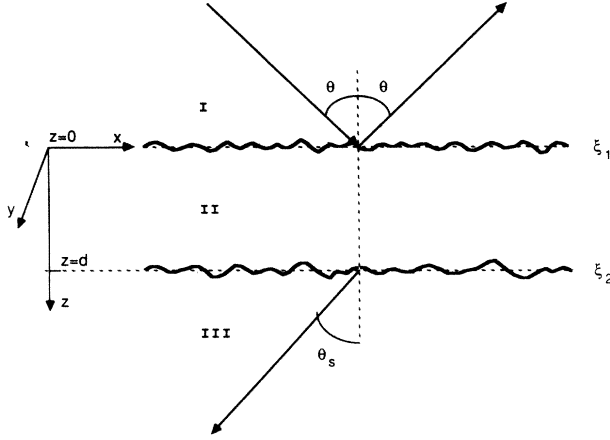


FIG. 8. Geometry used for the analysis of multilayer rough surfaces. Referring to the experimental situation, region I represents the prism + CaF<sub>2</sub> medium; region II, the Ag film surrounded by rough surfaces  $\xi_1$  and  $\xi_2$ ; and region III, vacuum. Planes  $z=0$  and  $z=d$  are placed on the average planes of surfaces  $\xi_1$  and  $\xi_2$ , respectively.

$z=d$  are the mean planes of the functions  $\xi_1$  and  $\xi_2$ , respectively. Incidence angle in region I is  $\theta$  and scattering angle in region II is  $\theta_s$ .

We assume an incident  $p$ -wave propagating in the  $x$ - $z$  plane with  $\mathbf{E}$  and  $\mathbf{H}$  fields defined by

$$\mathbf{E}(x,y,z) = \frac{1}{\omega\epsilon_1\epsilon_0} [k_1^0 \mathbf{k}_t^0 - (k_x^0)^2(0,0,1)] \times e^{-i(k_x^0 x + k_1^0 z)},$$

$$\mathbf{H}(x,y,z) = \mathbf{k}_1^0 e^{-i(k_x^0 x + k_1^0 z)},$$
(14)

where  $\mathbf{k}_t^0 = (k_x^0, 0, 0)$ ,  $\mathbf{k}_1^0 = (0, k_x^0, 0)$ , and  $k_x^0, k_1^0$  are the  $x, z$  components of the light wave vector, with  $k_1^0 = [(\omega^2/c^2)\epsilon_1 - (k_x^0)^2]^{1/2}$ . The superscript "0" is used to designate a wave vector for the incident wave. The Fourier transformed fields corresponding to Eq. (14) are

$$\mathbf{e}(\mathbf{k}, z) = \frac{1}{\omega\epsilon_1\epsilon_0} [k_1^0 \mathbf{k}_t^0 - (k_x^0)^2(0,0,1)] \times e^{-ik_1^0 z} \delta(\mathbf{k} - \mathbf{k}_t^0),$$

$$\mathbf{h}(\mathbf{k}, z) = \mathbf{k}_1^0 e^{-ik_1^0 z} \delta(\mathbf{k} - \mathbf{k}_t^0),$$
(15)

where  $\delta(\mathbf{k} - \mathbf{k}_t^0) = \delta(k_x - k_x^0)\delta(k_y)$  is the two-dimensional Dirac  $\delta$  function in  $\mathbf{k}$  space. We separate the  $p$  and  $s$  components of the reflected and transmitted Fourier transformed fields in regions I, II, and III according to

$$\mathbf{e}_{p_i}^\pm(\mathbf{k}, z) = \frac{p_i^\pm(\mathbf{k})}{\omega\epsilon_i\epsilon_0} [k_i \mathbf{k} \mp k^2(0,0,1)] e^{\mp ik_i z},$$

$$\mathbf{h}_{p_i}^\pm(\mathbf{k}, z) = \pm p_i^\pm(\mathbf{k}) \mathbf{k}_1 e^{\mp ik_i z},$$
(16)

$$\mathbf{e}_{s_i}^\pm(\mathbf{k}, z) = \mp s_i^\pm(\mathbf{k}) \mathbf{k}_1 e^{\mp ik_i z},$$
(17)

$$\mathbf{h}_{s_i}^\pm(\mathbf{k}, z) = \frac{s_i^\pm}{\omega\mu_0} [k_i \mathbf{k} \mp k^2(0,0,1)] e^{\mp ik_i z},$$

where  $k_i = [(\omega^2/c^2)\epsilon_i - k^2]^{1/2}$  for  $i=1,2,3$ . The  $\pm$  superscripts stand for  $\pm z$  propagation, respectively. For medium I only, the minus sign in Eqs. (16) and (17) is appropriate, and in medium III only, the plus sign applies. The symbols  $p_i^\pm$  and  $s_i^\pm$  represent the  $p$ - and  $s$ -wave amplitudes, respectively.

We are interested in obtaining the reflection coefficient for  $p$  waves and the angular distribution of  $p$ -polarized diffuse scattering intensity going into region III shown in Fig. 8. This can be obtained by solving the set of four linear equations which result from the application of the boundary conditions, given by Eqs. (10) and (12), to the smooth interfaces located at the planes  $z=0$  and  $z=d$ , shown in Fig. 8. This procedure is presented in some detail in the Appendix, and only the main results are given in the remainder of this section.

First, we consider a smooth multilayer system in Fig. 8 by setting  $\xi_1 = \xi_2 = 0$ . In this case, the coordinate space  $p$ -wave amplitudes are given by

$$\tilde{\mathbf{P}}(k_x^0) = \begin{pmatrix} P_1^-(k_x^0) \\ P_2^+(k_x^0) \\ P_2^-(k_x^0) \\ P_3^+(k_x^0) \end{pmatrix} = [\tilde{\mathbf{M}}_p(k_x^0)]^{-1} \tilde{\mathbf{p}}_0(k_x^0),$$
(18)

where  $\tilde{\mathbf{p}}_0(k_x^0)$  is a  $4 \times 1$  column matrix representing the excitation field and  $\tilde{\mathbf{M}}_p(k_x^0)$  is a  $4 \times 4$  matrix. Expressions for these matrices are given by Eqs. (A7) and (A3) in the Appendix, respectively. The complex SP wave vector,  $k_{SP} \equiv k'_{SP} + ik''_{SP}$ , is obtained from the solution of the determinantal equation

$$\det |\tilde{\mathbf{M}}_p(k_x^0)| \Big|_{k_x^0 = k_{SP}} = 0.$$
(19)

The reflected  $p$ -wave intensity is given by  $|P_1^-(k_x^0)|^2$  and will display a minimum for an incidence angle  $\theta = \theta_{\min}$  such that the wave-vector component  $k_x^0$  equals  $k'_{SP}$  [See Eq. (2)].

The SP damping is represented by the imaginary part of the SP wave-vector  $k_{SP}$ . It is related to the half-width  $\theta_{1/2}$  of the angular dependence of the reflectivity curve by<sup>19</sup>

$$\theta_{1/2} = -2(\tan\theta_{\min}) \frac{k''_{SP}}{k'_{SP}}.$$
(20)

Now, let us consider the multilayer rough surface shown in Fig. 8 with  $\xi_1$  and  $\xi_2 \neq 0$ . It is shown in the Appendix that to second order in  $\xi$ , Eq. (18) should be modified to

$$\tilde{\mathbf{P}}(k_x^0) = [\tilde{\mathbf{M}}_p(k_x^0) + \Delta\tilde{\mathbf{M}}_p(k_x^0)]^{-1} \times \left[ \frac{(2\pi)^2}{S_0} \tilde{\mathbf{j}}_0^{(2)}(k_x^0) + \tilde{\mathbf{p}}_0(k_x^0) \right],$$
(A31)

where  $S_0$  is the area illuminated by the incident beam and  $\tilde{j}_0^{(2)}(k_x^0)$  and  $\Delta\tilde{M}_p(k_x^0)$  are  $4 \times 1$  and  $4 \times 4$  matrices, respectively. These second-order correction terms are given by Eqs. (A25) and (A29) of the Appendix, respectively, and contain information on the roughness parameters of the two boundaries.

The effect of roughness on the SP dispersion relation is evident from Eq. (A31). The complex SP wave vector  $k_{SP}(\xi_1, \xi_2)$  now depends on  $\xi_1$  and  $\xi_2$  and is obtained from the solution of the determinantal equation:

$$\det \left[ \tilde{M}_p(k_x^0) + \Delta\tilde{M}_p(k_x^0) \right] \Big|_{k_x^0 = k_{SP}(\xi_1, \xi_2)} = 0 \quad (21)$$

which differs from the solution obtained from Eq. (19) due to the presence of the correction term  $\Delta\tilde{M}_p(k_x^0)$ .

The  $p$ -polarized scattered radiation in region III, expressed as a differential intensity per solid angle normalized to the incident intensity, for the case of uncorrelated rough surfaces  $\xi_1$  and  $\xi_2$  having Gaussian autocorrelation functions, is

$$\frac{1}{I_0} \frac{dI(\theta_s)}{d\Omega} = \frac{(2\pi)^2}{S_0} \frac{1}{n} \left[ \frac{2\pi}{\lambda} \right]^2 \frac{\cos^2\theta_s \sin^2\theta_s}{\cos\theta \sin^2\theta} |p_3^+(v_x)|^2 \quad (A33)$$

where  $n$  is the refractive index of the prism,  $v_x = (2\pi/\lambda)\sin\theta_s$ , and  $\theta_s$  is the scattering angle in the  $x$ - $z$  plane. The  $p$ -wave amplitude  $p_3^+(v_x)$  in Eq. (A33) incorporates the change in dispersion relation defined by Eq. (21) and is obtained from Eq. (A32) of the Appendix.

In Sec. IV, we will use the present formulation to interpret the experimental measurements. In addition, we will investigate the approximations that have been applied in the evaluation of  $k_{SP}(\xi_1, \xi_2)$ , and show that these approximations are invalid. Gaussian autocorrelation functions will be assumed for each rough surface in Fig. 8.

#### IV. RESULTS

In what follows, we will use the analysis developed in Sec. III to calculate the roughness parameters of the multilayer system studied in Ref. 12. The approximations incorporated into earlier models and the errors they introduce will be considered sequentially.

We shall first analyze the prediction for the modification in the dispersion relation of SP's for the case of a single interface and discuss briefly the numerical results of Sari and coworkers.<sup>18</sup> Sari and coworkers used the approach of Toigo *et al.*<sup>26</sup> and obtained an expression similar to Eq. (A42). However, they approximated the integrand in Eq. (A42) by extending the resonance condition for SP's for a smooth interface  $\alpha + \varepsilon\alpha_0 = 0$ , where  $\alpha$  and  $\alpha_0$  are the decay constants in the metal and dielectric regions, respectively, and  $\varepsilon$  is the metal complex permittivity, to all  $k$ -dependent variables which do not contribute to a pole in the integrand of Eq. (A42). Thus, the decay constants in each medium, represented by Eqs. (A43d) and (A43e), are assumed to satisfy the above relationship leading to the substitution  $\alpha' = -\varepsilon\alpha_0$  in the integrand of Eq. (A42).

We calculated  $\Delta k_{SP}$  from Eq. (A42) for the parameters

extracted from Ref. 12 for  $d_{CaF_2} = 1000 \text{ \AA}$  and we obtained the results shown in the third column of Table II.

Eliminating the Sari approximation results in smaller changes for  $\Delta\theta$  and  $\Delta\theta_{1/2}$ , giving an even greater discrepancy between theory and experiment. From Table II it is seen that the approximation is not valid, but there must be another reason for the disagreement. Sari's approximation is inappropriate because off-resonance values of  $k$  also contribute to the integral in Eq. (A42).

In Table II, the angular shift  $\Delta\theta$  and the increase in the linewidth of the ATR curve  $\Delta\theta_{1/2}$  are obtained from Eq. (A42) according to<sup>19</sup>

$$\Delta\theta = (\tan\theta_{\min}) \text{Re} \left[ \frac{\Delta k_{SP}}{k'_{SP}} \right],$$

$$\Delta\theta_{1/2} = -2(\tan\theta_{\min}) \text{Im} \left[ \frac{\Delta k_{SP}}{k'_{SP}} \right],$$

with  $\Delta k_{SP}$  given in Eq. (A42),  $k'_{SP} = (2\pi/\lambda)n \sin\theta_{\min}$ , and  $n$  is the prism refractive index used in Ref. 12. We calculated  $n = 1.461$  at  $\lambda = 4500 \text{ \AA}$  in order to match the minimum in the ATR curve for the smooth silver film in Ref. 12.

The above calculation is based on the determination of  $\delta$ ,  $\sigma$  from the scattering measurements of Ref. 12. For specular scattering, the theory should describe rather well the experiments for  $(2\pi\delta\sqrt{|\varepsilon|}/\lambda)^2 \ll 1$ , and this applies for the value of  $\delta$  extracted from Ref. 12. Therefore, the discrepancies in Table II suggest that those values of  $\delta$  and  $\sigma$  do not correspond to the real situation. In fact, there is a range of values of  $\delta$  and  $\sigma$  which describe the diffuse scattering measurements shown in Fig. 6 equally well. Consequently, to characterize the roughness parameters more precisely, one needs to make use of the data not only from diffuse but also from the specular scattering experiment.

Another source of error results from representing the rough surface by a single interface, i.e., assuming the silver film to have infinite thickness. The reason to consider the finite thickness is the strong dependence of the SP amplitude on this parameter as illustrated in Fig. 9. From this figure, whereas the resonance position remains practically unchanged for the different Ag thicknesses, the width and depth of the reflection minimum is strongly dependent on this parameter.<sup>32</sup> For large values of the metal thickness, an incident field couples very weakly with the SP and a small dip is observed in the reflected intensity. For small values of metal thickness, on the other hand, the excited mode loses its characteristics of a localized surface mode and the reflected intensity does not display a well-defined resonance. For intermediate thickness values, the SP is more strongly coupled to the incident field. In the case of silver at  $\lambda = 6328 \text{ \AA}$  a film thickness of  $500 \text{ \AA}$  gives an optimum coupling. The behavior of the ATR curves shown in Fig. 9 indicates that the amount of loss to other modes due to roughness, which depends on the strength of the SP amplitude, will be a function of the metal thickness.

Let us assume, initially, only the presence of the silver-vacuum roughness, described by the parameters  $\delta_2$

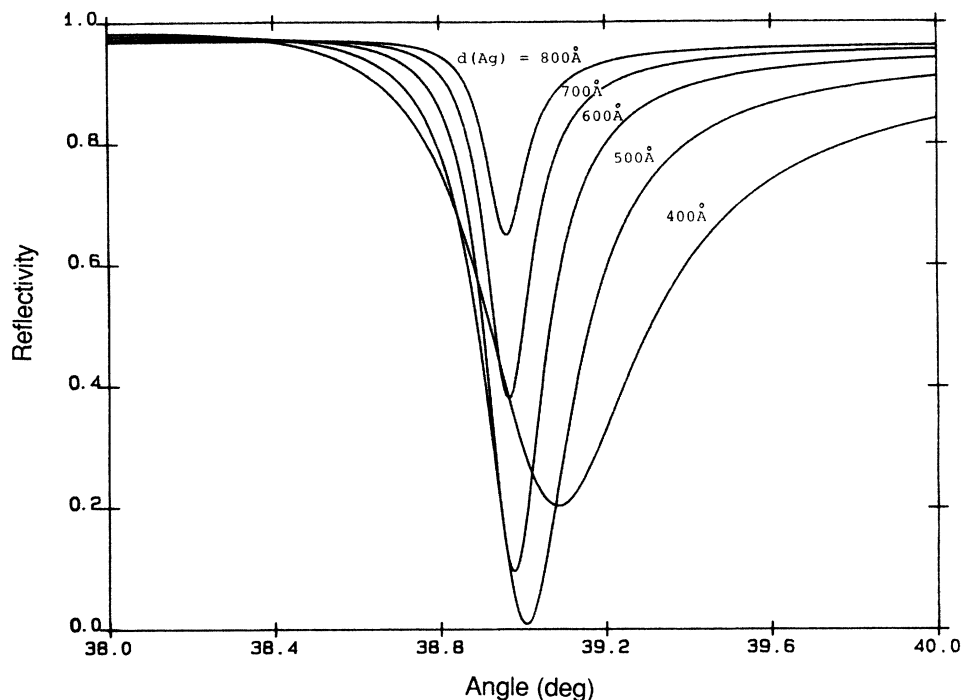


FIG. 9. ATR curves of silver films at  $\lambda = 6328 \text{ \AA}$  for different thicknesses.

and  $\sigma_2$ , in the configuration of Fig. 8. Considering the experimental value for the shift in the minimum position  $\Delta\theta = 2^\circ$  in Table III, we calculate the locus of points  $(\delta_2, \sigma_2)$  which yield this value for  $\Delta\theta$ . (For these calculations the thickness of the silver film is taken to be  $500 \text{ \AA}$ .) This curve is shown in Fig. 10 (curve A), and was obtained with the use of Eq. (A31) with  $\xi_1 = 0$  (i.e., no  $\text{CaF}_2$ -Ag interface roughness). Similarly, we calculated from Eq. (A33) the set of points  $(\delta_2, \sigma_2)$  which yield the same maximum diffuse scattered intensity (which occurs at  $\approx -45^\circ$ ), as shown in the experimental curve of Fig. 6. This curve of constant maximum intensity is shown in Fig. 10 as curve C. From the intersection of curves A and C the values  $\delta_2 = 40 \text{ \AA}$  and  $\sigma_2 = 127 \text{ \AA}$  are obtained.

Figure 11 displays the experimental ATR curve of Fig. 4 together with the theoretical prediction obtained from Eq. (A31) for  $\delta_2$  and  $\sigma_2$  given above. From this figure,

even though the calculated parameters give the correct resonance position, the increase in  $\Delta\theta_{1/2}$ , the half-width, is less than half of the observed value. Nevertheless, it represents an order magnitude improvement as compared to the calculated width increase that would be obtained from the single interface calculation (as performed by Raether<sup>19</sup>) for these roughness parameters. However, the shift in the minimum position of the ATR curve  $\Delta\theta$ , is not significantly affected by the thickness of the silver film. These comparisons support our previous remarks concerning the role of the thickness in the change of the dispersion of SP's.

The angular dependence of the diffusely scattered *p*-polarized intensity in the vacuum region is shown in Fig. 12 for  $\delta_2 = 40 \text{ \AA}$  and  $\sigma_2 = 127 \text{ \AA}$ , together with the measured curve extracted from the experiment of Ref. 12. The theory describes the experiment rather well in the

TABLE III. Specular reflection parameters for a single rough interface between two semi-infinite media, a single rough interface with finite thickness, and a two-layer rough surface. ( $\lambda = 4500 \text{ \AA}$ .)

	Experimental	Single interface assumption with Sari approximation	Single rough interface with finite thickness and removing the Sari approximation	Two-layer rough surface analysis
$d_{\text{CaF}_2} = 1000 \text{ \AA}$		$\delta_1 = 0, \delta_2 = 40 \text{ \AA}$	$\delta_1 = 0, \delta_2 = 40 \text{ \AA}$	$\delta_1 = 93 \text{ \AA}, \delta_2 = 39 \text{ \AA}$
Ref. 12		$\sigma_1 = 0, \sigma_2 = 127 \text{ \AA}$ $d = \infty$	$\sigma_1 = 0, \sigma_2 = 127 \text{ \AA}$ $d = 500 \text{ \AA}$	$\sigma_1 = 1000 \text{ \AA}, \sigma_2 = 135 \text{ \AA}$ $d = 500 \text{ \AA}$
$\Delta\theta$ (deg)	2	1.6	2	2
$\Delta\theta_{1/2}$ (deg)	1.75	0.06	0.7	1.5

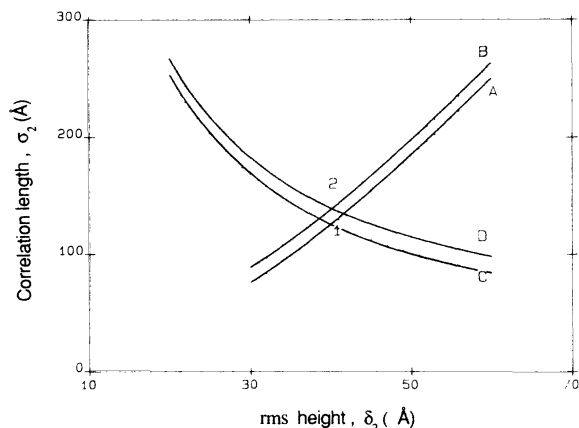


FIG. 10. Graphic method for finding multilayer rough surface parameters. Without the inclusion of the  $\text{CaF}_2$ -Ag rough surface, the locus of silver-vacuum roughness parameters ( $\delta_2, \sigma_2$ ), yielding a shift  $\Delta\theta = 2^\circ$  in the ATR curve, is represented by curve *A*. Curve *C* is the locus of points giving the same maximum of diffuse scattered intensity, corresponding to the value obtained in the experiment. The intersection of these two curves occurs at point 1. The inclusion of the  $\text{CaF}_2$ -Ag rough surface results in curves *B* and *D*, so that the intersection is moved to point 2. The resulting set of parameters is  $\delta_{\text{Ag}} = 39 \text{ \AA}$ ,  $\sigma_{\text{Ag}} = 135 \text{ \AA}$ ,  $\delta_{\text{CaF}_2} = 93 \text{ \AA}$ ,  $\sigma_{\text{CaF}_2} = 1000 \text{ \AA}$ , giving the best fit to both diffuse and specular intensity curves. For these calculations the thickness of the silver film is taken to be  $500 \text{ \AA}$ .

backward direction, but discrepancies still remain for positive values of scattering angle. It is interesting to note that even though the parameters  $\delta_2$  and  $\sigma_2$  differ greatly from the corresponding ones obtained in Ref. 12, they give a description of the diffuse scattering data which does not differ significantly from the theoretical prediction of Ref. 12, as can be seen by comparing the theoretical curves of Figs. 6 and 12.

To account for the remaining differences between theory and experiment we have included the effect of the  $\text{CaF}_2$ -Ag interface roughness in our calculations. As can

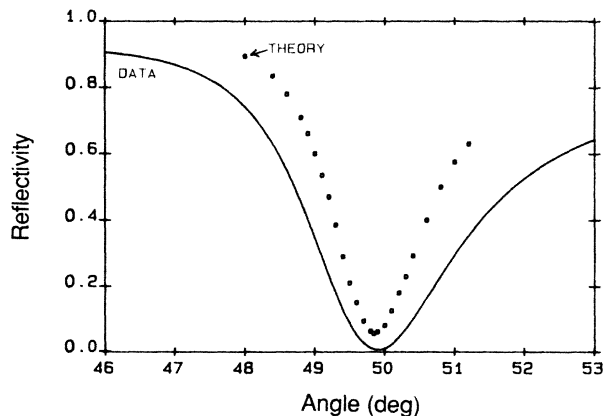


FIG. 11. ATR curves for Ag film with underlayer of  $\text{CaF}_2$ , with the data represented by a solid line. Dots represent the theoretical prediction with  $\delta_2 = 40 \text{ \AA}$ ,  $\sigma_2 = 125 \text{ \AA}$ ,  $\delta_1 = 0 \text{ \AA}$ , and for the optical parameters of the smooth Ag film of Ref. 12.

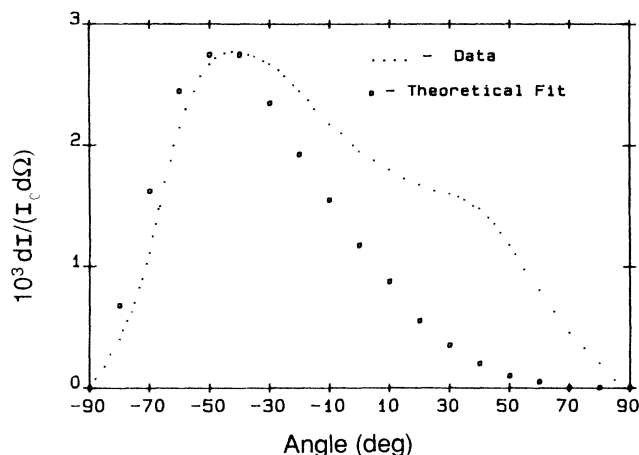


FIG. 12. Diffuse scattering intensity curves for Ag on  $\text{CaF}_2$  ( $1000 \text{ \AA}$ ). Dotted curve is the data from Ref. 12. Small circles represent the theoretical prediction for the parameters given in Fig. 11.

be observed in Fig. 12 the discrepancy between the theoretical and experimental curves shows up for positive angles, suggesting that the  $\text{CaF}_2$ -Ag interface roughness is characterized by correlation lengths which are larger than the value calculated in Fig. 10 for the Ag-vacuum roughness. As a result, we have assumed for simplicity no correlation between the two rough surfaces which define the boundaries of the silver film. This lack of correlation was taken into account in our calculations by neglecting, in the theoretical expressions of Eqs. (A31) and (A33), the cross products containing terms of the form  $\hat{\xi}_i(\mathbf{k} - \mathbf{k}_i^0)\hat{\xi}_j(\mathbf{k}_i^0 - \mathbf{k})$ , with  $i, j = 1, 2$ , and  $i \neq j$ .

With the  $\text{CaF}_2$ -Ag interface roughness included, described by the parameters  $\delta_1$  and  $\sigma_1$ , the curves *A* and *C* of Fig. 10 are modified depending on the values of these parameters. These modifications are shown in Fig. 10 as curves *B* and *D* for  $\sigma_1 = 1000 \text{ \AA}$  and  $\delta_1 = 93 \text{ \AA}$ . The particular values chosen for  $\sigma_1$  and  $\delta_1$  provide the best agreement between theory and experiment. From Fig. 10 the effect of the  $\text{CaF}_2$ -Ag interface roughness is to move the intersection from point 1 to point 2, which corresponds to  $\approx 6\%$  change in the values of  $\delta_2$  and  $\sigma_2$  which were obtained by assuming a smooth  $\text{CaF}_2$ -Ag interface.

The effect of the  $\text{CaF}_2$ -Ag interface roughness is clearly demonstrated in the specular and diffuse scattering curves shown in Figs. 13 and 14, which are calculated for  $\delta_1 = 93 \text{ \AA}$ ,  $\sigma_1 = 1000 \text{ \AA}$ ,  $\delta_2 = 39 \text{ \AA}$ , and  $\sigma_2 = 135 \text{ \AA}$ . An examination of these curves shows that the experimental data can be reproduced with excellent accuracy by allowing for roughness at the  $\text{CaF}_2$ -Ag interface. One should notice that the roughness parameters obtained in the present calculation for the  $\text{CaF}_2$ -Ag interface are well within the range observed from electron micrographs of the surface of  $\text{CaF}_2$  films deposited under similar conditions.<sup>20</sup>

In summary, three inappropriate approximations were introduced into the theoretical model.

- (1) The resonance relationship between the two decay

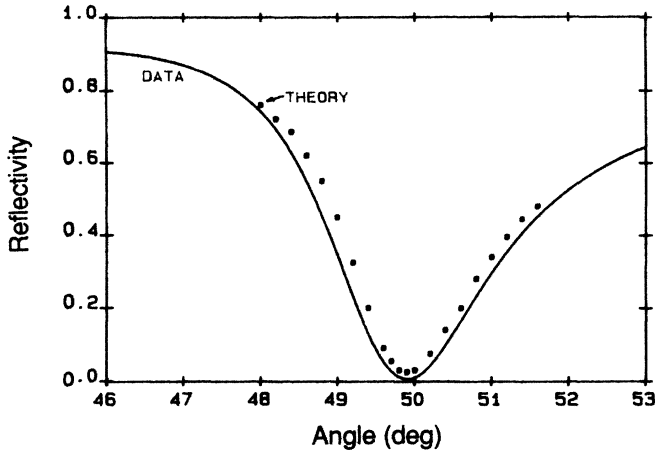


FIG. 13. Comparison between theory and experiment for specular reflection intensity from Ag on  $\text{CaF}_2$  (1000 Å). The theory curve is for the parameter values  $\delta_1=93\text{Å}$ ,  $\sigma_1=1000\text{Å}$ ,  $\delta_2=39\text{Å}$ , and  $\sigma_2=135\text{Å}$ , obtained by fitting the model to the data.

constants in the  $z$  direction (into the metal and into the dielectric) was extended to all  $k$  values (i.e., the Sari approximation.)

(2) The metal film was assumed to have infinite thickness.

(3) A consequence of (2) is the neglect of the rough surface between the  $\text{CaF}_2$  and the Ag.

Table III presents the experimental data for the specular measurements, with theoretical calculations illustrating the effects of the above approximations.

## V. CONCLUSIONS

We have presented a theoretical analysis for the problem of scattering and dispersion of SP's excited by the ATR technique in rough metal films using the surface current approach. Our results are applied to the calcula-

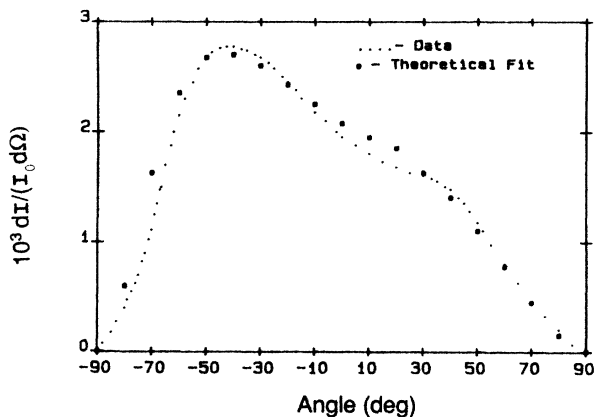


FIG. 14. Comparison between theory and experiment for diffuse scattered intensity from Ag on  $\text{CaF}_2$  (1000 Å). The theoretical calculations use the parameters given for Fig. 13.

tion of the roughness parameters for a particular experiment where specular and diffuse scattering data on the same sample were available.

It has been shown that earlier estimates for the change in the dispersion relation of SP's based on the single interface calculations of Sari and co-workers were not appropriate because the resonance approximation used by these authors overestimates the shift in the wave vector and leads to wrong results for the damping of SP's. We performed calculations for the same single-interface problem with use of the roughness parameters extracted from the diffuse scattering measurements, as calculated by Hornauer,<sup>12</sup> and showed that these parameters did not describe the experimental situation. Contrary to previous treatments, we found that both specular and diffuse scattering data must be taken into account to obtain consistent roughness parameters.

We evaluated contributions to the theoretical calculations by including the effect of the finite Ag film thickness as used in the experiments. Even though the SP wave vector is rather insensitive to thickness variations, the same is not true for the amplitude of the wave. As a result, for the case of a rough metal film, the amount of loss to other modes, which accounts for much of the increase in the half-width of the ATR curve, does depend on the film thickness.

Furthermore, we demonstrated that the presence of the  $\text{CaF}_2$ -Ag interface roughness plays an important role in the description of the specular and diffuse scattering data, mostly to explain the diffuse scattered intensity distribution in the forward direction and the increase in linewidth of the ATR curve. The results of our analysis also demonstrate that the roughness parameters of the  $\text{CaF}_2$  film, which is hidden under the silver film in the experiments, are also determined from the specular and diffuse scattering measurements, and hence the technique can be used to characterize multilayer rough surfaces.

Although the inclusion of the  $\text{CaF}_2$ -Ag interface roughness gives a remarkably good prediction for the specular and diffuse scattering curves, it introduces only a 6% correction in the roughness parameters of the Ag-vacuum interface calculated with the assumption of the  $\text{CaF}_2$ -Ag interface being smooth. This suggests that the Ag-vacuum roughness parameters, for the case where the different surface structures are resolvable, can be determined quite accurately by a measurement of the resonance position of the specular and the intensity maximum of the diffuse scattering.

In summary, we have shown that the apparent inconsistency between theory and experiment as pointed out in previous works is non-existent, and that SPS can, indeed, be used to characterize not only single layer but also multilayer rough surfaces.

## ACKNOWLEDGMENTS

We would like to thank Dr. J. Feinstein of the Electrical Engineering Department at Stanford University for valuable discussions in the beginning of this work. One of us (E. Fontana) is supported by a grant from Coordenadoria de Aperfeiçoamento de Pessoal de Ensino Superior (CAPES), Brazil.

**APPENDIX: CALCULATION OF SPECULAR  
AND DIFFUSE SCATTERING INTENSITIES  
FROM MULTILAYER ROUGH SURFACES  
INCLUDING PLASMON EFFECTS**

**A. Specular reflection intensity**

To solve for the reflected and transmitted  $p$ - and  $s$ -wave amplitudes, we combine Eqs. (10) and (12) with Eqs.

(16) and (17) to obtain two sets of four simultaneous equations which can be written in matrix form as

$$\tilde{M}_p(k)\tilde{p}(\mathbf{k}) = \tilde{j}_p(\mathbf{k}) + \tilde{p}_0(\mathbf{k}_1^0)\delta(\mathbf{k} - \mathbf{k}_1^0), \quad (\text{A1})$$

$$\tilde{M}_s(k)\tilde{s}(\mathbf{k}) = \omega\mu_0\tilde{j}_s(\mathbf{k}), \quad (\text{A2})$$

with

$$\tilde{M}_p(k) = \begin{pmatrix} 1 & 1 & -1 & 0 \\ k_1/\varepsilon_1 & -k_2/\varepsilon_2 & -k_2/\varepsilon_2 & 0 \\ 0 & -e^{-ik_2d} & e^{ik_2d} & e^{-ik_3d} \\ 0 & \frac{k_2}{\varepsilon_2}e^{-ik_2d} & \frac{k_2}{\varepsilon_2}e^{ik_2d} & -\frac{k_3}{\varepsilon_3}e^{-ik_3d} \end{pmatrix}, \quad (\text{A3})$$

$$\tilde{M}_s(k) = \begin{pmatrix} 1 & 1 & -1 & 0 \\ k_1 & -k_2 & -k_2 & 0 \\ 0 & -e^{-ik_2d} & e^{ik_2d} & e^{-ik_3d} \\ 0 & k_2e^{-ik_2d} & k_2e^{ik_2d} & -k_3e^{-ik_3d} \end{pmatrix}, \quad (\text{A4})$$

$$\tilde{p}(\mathbf{k}) = \begin{pmatrix} p_1^-(\mathbf{k}) \\ p_2^+(\mathbf{k}) \\ p_2^-(\mathbf{k}) \\ p_3^+(\mathbf{k}) \end{pmatrix}, \quad \tilde{s}(\mathbf{k}) = \begin{pmatrix} s_1^-(\mathbf{k}) \\ s_2^+(\mathbf{k}) \\ s_2^-(\mathbf{k}) \\ s_3^+(\mathbf{k}) \end{pmatrix}, \quad (\text{A5})$$

$$\tilde{j}_p(\mathbf{k}) = \begin{pmatrix} j_{p1}(\mathbf{k}) \\ j_{z1}(\mathbf{k}) \\ j_{p2}(\mathbf{k}) \\ j_{z2}(\mathbf{k}) \end{pmatrix}, \quad \tilde{j}_s(\mathbf{k}) = \begin{pmatrix} 0 \\ j_{s1}(\mathbf{k}) \\ 0 \\ j_{s2}(\mathbf{k}) \end{pmatrix}, \quad (\text{A6})$$

$$\tilde{p}_0(\mathbf{k}_1^0) = \begin{pmatrix} 1 \\ -k_1^0/\varepsilon_1 \\ 0 \\ 0 \end{pmatrix}. \quad (\text{A7})$$

The next step is to determine the source currents in Eq. (A6). From Eq. (6), these are given by

$$\begin{aligned} \mathbf{j}_1(\mathbf{k}) &= i\omega\varepsilon_0 \int d\mathbf{q} [(\varepsilon_1 - 1)\mathbf{e}_1(\mathbf{q}, 0) - (\varepsilon_2 - 1)\mathbf{e}_2(\mathbf{q}, 0)] \hat{\xi}_1(\mathbf{k} - \mathbf{q}), \\ \mathbf{j}_2(\mathbf{k}) &= i\omega\varepsilon_0 \int d\mathbf{q} [(\varepsilon_2 - 1)\mathbf{e}_2(\mathbf{q}, d) - (\varepsilon_3 - 1)\mathbf{e}_3(\mathbf{q}, d)] \hat{\xi}_2(\mathbf{k} - \mathbf{q}), \end{aligned} \quad (\text{A8})$$

where  $\mathbf{q} = (q_x, q_y, 0)$  is a wave vector in the  $x$ - $y$  plane,  $\mathbf{j}_1$  is the current source at the interface of regions I and II in Fig. 8, and  $\mathbf{j}_2$  is the current source between regions II and III. From the definitions of  $j_p$  and  $j_s$  given by Eqs. (11) and (13), respectively, we obtain for the source currents of Eq. (A6).

$$\tilde{j}_p(\mathbf{k}) = i \int d\mathbf{q} \tilde{\xi}(\mathbf{k} - \mathbf{q}) \left[ \tilde{A}_1(\mathbf{k}, \mathbf{q}) + \frac{k_y q_y}{k^2} \tilde{A}_2(q) \right] \tilde{p}(\mathbf{q}) + \tilde{j}_{p0}(k) \quad (\text{A9})$$

and

$$\tilde{j}_s(\mathbf{k}) = i \int d\mathbf{q} \left[ \frac{k_x q_x - k_y q_y}{k^2} \right] \tilde{\xi}(\mathbf{k} - \mathbf{q}) \tilde{A}_3(q) \tilde{p}(\mathbf{q}) + \tilde{j}_{s0}(\mathbf{k}), \quad (\text{A10})$$

where

$$\tilde{\xi}(\mathbf{k}-\mathbf{q}) = \begin{pmatrix} \hat{\xi}_1(\mathbf{k}-\mathbf{q}) & 0 & 0 & 0 \\ 0 & \hat{\xi}_1(\mathbf{k}-\mathbf{q}) & 0 & 0 \\ 0 & 0 & \hat{\xi}_2(\mathbf{k}-\mathbf{q}) & 0 \\ 0 & 0 & 0 & \hat{\xi}_2(\mathbf{k}-\mathbf{q}) \end{pmatrix}, \quad (\text{A11})$$

$$\tilde{A}_1(\mathbf{k}, \mathbf{q}) = \begin{pmatrix} \frac{\epsilon_1-1}{\epsilon_1} \frac{q_x k_x q_1}{k_2} & -\frac{(\epsilon_2-1)}{\epsilon_2} \frac{q_x k_x q_2}{k^2} & -\frac{(\epsilon_2-1)}{\epsilon_2} \frac{q_x k_x q_2}{k^2} & 0 \\ \frac{\epsilon_1-1}{\epsilon_1} q^2 & \frac{\epsilon_2-1}{\epsilon_2} q^2 & -\frac{(\epsilon_2-1)}{\epsilon_2} q^2 & 0 \\ 0 & \frac{\epsilon_2-1}{\epsilon_2} \frac{q_x k_x q_2}{k^2} e^{-iq_2 d} & \frac{\epsilon_2-1}{\epsilon_2} \frac{q_x k_x q_2}{k^2} e^{iq_2 d} & -\frac{(\epsilon_3-1)}{\epsilon_3} q_x k_x q_3 e^{-iq_3 d} \\ 0 & -\frac{(\epsilon_2-1)}{\epsilon_2} q^2 e^{-iq_2 d} & \frac{\epsilon_2-1}{\epsilon_2} q^2 e^{iq_2 d} & \frac{\epsilon_3-1}{\epsilon_3} q^2 e^{-iq_3 d} \end{pmatrix},$$

$$q_i = \left[ \frac{\omega^2}{c^2} \epsilon_i - q^2 \right]^{1/2}, \quad i=1,2,3 \quad (\text{A12})$$

$$\tilde{A}_2(q) = \begin{pmatrix} \frac{\epsilon_1-1}{\epsilon_1} q_1 & -\frac{(\epsilon_2-1)}{\epsilon_2} q_2 & -\frac{(\epsilon_2-1)}{\epsilon_2} q_2 & 0 \\ 0 & 0 & 0 & 0 \\ 0 & \frac{\epsilon_2-1}{\epsilon_2} q_2 e^{-iq_2 d} & \frac{\epsilon_2-1}{\epsilon_2} q_2 e^{iq_2 d} & -\frac{(\epsilon_3-1)}{\epsilon_3} q_3 e^{-iq_3 d} \\ 0 & 0 & 0 & 0 \end{pmatrix}, \quad (\text{A13})$$

$$\tilde{A}_3(q) = \begin{pmatrix} 0 & 0 & 0 & 0 \\ \frac{\epsilon_1-1}{\epsilon_1} q_1 & -\frac{(\epsilon_2-1)}{\epsilon_2} q_2 & -\frac{(\epsilon_2-1)}{\epsilon_2} q_2 & 0 \\ 0 & 0 & 0 & 0 \\ 0 & \frac{\epsilon_2-1}{\epsilon_2} q_2 e^{-iq_2 d} & \frac{\epsilon_2-1}{\epsilon_2} q_2 e^{iq_2 d} & -\frac{(\epsilon_3-1)}{\epsilon_3} q_3 e^{-iq_3 d} \end{pmatrix}, \quad (\text{A14})$$

$$\tilde{j}_{p0}(\mathbf{k}) = i \left[ \frac{\epsilon_1-1}{\epsilon_1} \right] \hat{\xi}_1(\mathbf{k}-\mathbf{k}_t^0) \begin{pmatrix} k_x k_1^0 k_x^0 / k^2 \\ -(k_x^0)^2 \\ 0 \\ 0 \end{pmatrix}, \quad (\text{A15})$$

$$\tilde{j}_{s0}(\mathbf{k}) = -i \left[ \frac{\epsilon_1-1}{\epsilon_1} \right] \frac{k_y k_1^0 k_x^0}{k^2} \hat{\xi}_1(\mathbf{k}-\mathbf{k}_t^0) \begin{pmatrix} 0 \\ 1 \\ 0 \\ 0 \end{pmatrix}. \quad (\text{A16})$$

The amplitudes of the  $p$  and  $s$  waves are obtained by the substitution of Eqs. (A9) and (A10) into Eqs. (A1) and (A2)

$$\tilde{p}(\mathbf{k}) = \tilde{M}_p^{-1}(k) \left\{ i \int d\mathbf{q} \left[ \tilde{\xi}(\mathbf{k}-\mathbf{q}) \left[ \tilde{A}_1(\mathbf{k}, \mathbf{q}) + \frac{k_y q_y}{k^2} \tilde{A}_2(q) \right] \tilde{p}(\mathbf{q}) \right] + \tilde{p}_0(\mathbf{k}) \delta(\mathbf{k}-\mathbf{k}_t^0) + \tilde{j}_{p0}(\mathbf{k}) \right\}, \quad (\text{A17})$$

$$\tilde{s}(\mathbf{k}) = \omega \mu_0 \tilde{M}_s^{-1}(k) \left\{ i \int d\mathbf{q} \left[ \left[ \frac{k_x q_y - k_y q_x}{k^2} \right] \tilde{\xi}(\mathbf{k}-\mathbf{q}) \tilde{A}_3(q) \tilde{p}(\mathbf{q}) \right] + \tilde{j}_{s0}(\mathbf{k}) \right\}, \quad (\text{A18})$$

where  $\tilde{M}_p^{-1}(k)$  in Eq. (A17) is the inverse matrix of  $\tilde{M}_p(k)$  given by Eq. (A3). The magnitude of the determinant of  $\tilde{M}_p^{-1}$  is a minimum when the dispersion relation of the SP for a smooth multilayer system in the geometry of Fig. 8 is

fulfilled. The matrix  $\tilde{M}_s^{-1}$  in Eq. (A18) is the inverse of  $\tilde{M}_s$ , given by Eq. (A4), and the elements of  $\tilde{M}_s^{-1}$  do not display any resonant behavior.

To analyze the effect of the roughness on the  $p$ -wave amplitudes to first order in  $\xi$ , we note that the most significant contribution to the integral on the right-hand side (rhs) of Eq. (A17) occurs when  $\mathbf{q} \simeq \mathbf{k}_i^0$ . Hence, we substitute for  $\tilde{p}(\mathbf{q})$  on the rhs of Eq. (A17) the zero-order solution corresponding to a smooth multilayer system in Fig. 8, and which is obtained from Eq. (A17) by setting  $\xi$  equal to zero. That is,

$$\tilde{p}(\mathbf{q}) = \tilde{p}^{(0)}(\mathbf{q}) = \tilde{M}_p^{-1}(q) \tilde{p}_0(\mathbf{q}) \delta(\mathbf{q} - \mathbf{k}_i^0). \quad (\text{A19})$$

The substitution of Eq. (A19) into Eq. (A17) gives the first-order correction

$$\tilde{p}(\mathbf{k}) = \tilde{p}^{(0)}(\mathbf{k}) + \tilde{p}^{(1)}(\mathbf{k}), \quad (\text{A19}')$$

where

$$\tilde{p}^{(1)}(\mathbf{k}) = \tilde{M}_p^{-1}(k) [\tilde{j}_{p0}(\mathbf{k}) + i \tilde{\xi}(\mathbf{k} - \mathbf{k}_i^0) \tilde{A}_1(\mathbf{k}, k_i^0) \tilde{M}_p^{-1}(k_x^0) \tilde{p}_0(\mathbf{k}_i^0)]. \quad (\text{A20})$$

For  $\mathbf{k} \neq \mathbf{k}_i^0$ ,  $\tilde{p}^{(0)}(\mathbf{k}) = 0$ , so that in the nonspecular direction, amplitudes are given by Eq. (A20). In the specular direction, the first-order modification given by Eq. (A20) yields

$$\tilde{p}^{(1)}(\mathbf{k}_i^0) = \tilde{M}_p^{-1}(k_x^0) [i \tilde{\xi}(\mathbf{0}) \tilde{A}_1(k_x^0, k_x^0) \tilde{M}_p^{-1}(k_x^0) \tilde{p}_0(k_i^0) + \tilde{j}_0(k_i^0)].$$

The terms  $\tilde{j}_0(\mathbf{k}_i^0)$  and  $\tilde{\xi}(\mathbf{0})$  involve the spatial averages  $\langle \xi_1 \rangle$  and  $\langle \xi_2 \rangle$  of the surface profiles, and since we located the planes  $z=0$  and  $z=d$  on the average planes,  $\tilde{p}^{(1)}(\mathbf{k}_i^0) = 0$ . Hence, to first order, the roughness does not modify the  $p$ -wave amplitudes in the specular direction, in agreement with previous results.<sup>14,22</sup>

To obtain the modification of the specular  $p$ -wave amplitudes, we extend the calculations to second order. In this case, in addition to the  $p$ -wave amplitudes given in Eq. (A17)  $s$ -wave amplitudes are also present, as given by Eq. (A18). By using the same procedure that led to Eq. (A10), we obtain a second-order expression for  $\tilde{j}_p(\mathbf{k})$ , including the  $p$ - and  $s$ -wave amplitudes:

$$\tilde{j}_p(\mathbf{v}) = \left\{ i \int d\mathbf{k} \tilde{\xi}(\mathbf{v} - \mathbf{k}) \left[ \left[ \tilde{A}_1(\mathbf{v}, \mathbf{k}) + \frac{v_y k_y}{v^2} \tilde{A}_2(k) \right] \tilde{p}(k) + \omega \epsilon_0 \left[ \frac{v_x k_y - v_y k_x}{v^2} \right] \tilde{A}_4(k) \tilde{s}(\mathbf{k}) \right] + \tilde{j}_{p0}(\mathbf{v}) \right\}, \quad (\text{A21})$$

where  $\mathbf{v} = (v_x, v_y, 0)$  is a two-component wave vector and

$$\tilde{A}_4(k) = \begin{pmatrix} -(\epsilon_1 - 1) & -(\epsilon_2 - 1) & (\epsilon_2 - 1) & 0 \\ 0 & 0 & 0 & 0 \\ 0 & (\epsilon_2 - 1)e^{-ik_2 d} & -(\epsilon_2 - 1)e^{ik_2 d} & -(\epsilon_2 - 1)e^{-ik_3 d} \\ 0 & 0 & 0 & 0 \end{pmatrix}, \quad (\text{A22})$$

$$k_i = \left[ \frac{\omega^2}{c^2} \epsilon_i - k^2 \right]^{1/2}, \quad i = 1, 2, 3.$$

Substituting Eqs. (A17) and (A18) into Eq. (A21) one obtains, to second order, the current source representing the excitation of a  $p$ -wave mode with wave-vector component  $\mathbf{v}$  in the  $x$ - $y$  plane

$$\tilde{j}_p(\mathbf{v}) = \tilde{j}_0^{(1)}(\mathbf{v}) + \tilde{j}_0^{(2)}(\mathbf{v}) + \tilde{j}_p^{(1)}(\mathbf{v}) + \tilde{j}_p^{(2)}(\mathbf{v}) \quad (\text{A23})$$

with

$$\tilde{j}_0^{(1)}(\mathbf{v}) = \tilde{j}_{p0}(\mathbf{v}), \quad (\text{A24})$$

where  $\tilde{j}_{p0}(\mathbf{v})$  is obtained from Eq. (A15) by making  $\mathbf{k} \rightarrow \mathbf{v}$ ,

$$\tilde{j}_0^{(2)}(\mathbf{v}) = i \int d\mathbf{k} \tilde{\xi}(\mathbf{v} - \mathbf{k}) \left[ \left[ \tilde{A}_1(\mathbf{v}, \mathbf{k}) + \frac{v_y k_y}{v^2} \tilde{A}_2(k) \right] \tilde{M}_p^{-1}(k) \tilde{j}_{p0}(\mathbf{k}) + \frac{\omega^2}{c^2} \left[ \frac{v_x k_y - v_y k_x}{k^2} \right] \tilde{A}_4(k) \tilde{M}_s^{-1}(k) j_{s0}(\mathbf{k}) \right], \quad (\text{A25})$$

$$\tilde{j}_p^{(1)}(\mathbf{v}) = i \tilde{\xi}(\mathbf{v} - \mathbf{k}_i^0) \tilde{A}_1(\mathbf{v}, \mathbf{k}_i^0) \tilde{M}_p^{-1}(k_x^0) \tilde{p}_0(\mathbf{k}_i^0), \quad (\text{A26})$$

$$\begin{aligned} \tilde{j}_p^{(2)}(\mathbf{v}) = & - \int \int d\mathbf{k} d\mathbf{q} \tilde{\xi}(\mathbf{v}-\mathbf{k}) \left[ \left[ \tilde{A}_1(\mathbf{v}, \mathbf{k}) + \frac{v_y k_y}{v^2} \tilde{A}_2(k) \right] \tilde{M}_p^{-1}(k) \tilde{\xi}(\mathbf{k}-\mathbf{q}) \left[ \tilde{A}_1(\mathbf{k}, \mathbf{q}) + \frac{k_y q_y}{k^2} \tilde{A}_2(q) \right] \right. \\ & \left. + \frac{\omega^2}{c^2} \left[ \frac{v_x k_y - v_y k_x}{v^2} \right] \left[ \frac{k_x q_y - k_y q_x}{k^2} \right] \tilde{A}_4(k) \tilde{M}_s^{-1}(k) \tilde{\xi}(\mathbf{k}-\mathbf{q}) \tilde{A}_3(q) \right] \tilde{p}(\mathbf{q}). \end{aligned} \quad (\text{A27})$$

The term  $\tilde{j}_0^{(1)}(\mathbf{v})$  in Eq. (A23) is the first-order current source for the  $p$  waves with wave-vector component  $\mathbf{v}$  in the plane  $x$ - $y$ , produced by the driving field. The current term  $\tilde{j}_0^{(2)}(\mathbf{v})$  is the sum of two terms. The first one is the current source produced by a second-order process which originates with the driving field and has, as an intermediate step, the generation of a  $p$ -wave mode with wavevector component  $\mathbf{k}$  on the  $x$ - $y$  plane. The second term on the rhs of Eq. (A25) results from a process similar to the previous one, but having, as the intermediate step, the production of an  $s$ -wave mode with wave-vector  $\mathbf{k}$  in the  $x$ - $y$  plane. The term  $\tilde{j}_p^{(1)}(\mathbf{v})$ , is the first-order current produced by the specular  $p$ -wave amplitudes and those are calculated for the smooth multilayer system in Fig. 8. The term  $\tilde{j}_p^{(2)}(\mathbf{v})$  is the result of all second-order processes which start at a given  $p$  wave with wave-vector component  $\mathbf{q}$  in the  $x$ - $y$  plane and have, as the intermediate step, the generation of a  $p$ -wave and  $s$ -wave mode with wave-vector component  $\mathbf{k}$  in the  $x$ - $y$  plane, represented by the first and second terms on the rhs of Eq. (A27), respectively.

For the source term  $\tilde{j}_p^{(2)}(\mathbf{v})$  we isolate from the  $\mathbf{q}$  space, contributions to the  $\mathbf{q}$  integral over a small region around  $\mathbf{q} \sim \mathbf{v}$ . Over this region, we make  $\int d\mathbf{q} \tilde{f}(\mathbf{q}) \sim [(2\pi)^2/S_0] \tilde{f}(\mathbf{v})$ , where  $S_0$  is the illuminated area and  $\tilde{f}(\mathbf{v})$  is the integrand in Eq. (A27) for  $\mathbf{q}=\mathbf{v}$ . An inspection of Eq. (A27) shows that this contribution will have an effect on the matrix elements of  $\tilde{M}_p(\mathbf{v})$ , whose importance will depend on the size of the elements of  $\tilde{M}_p(\mathbf{v})$ . The rest of the integral in  $\mathbf{q}$  is of higher order in comparison to the first- and second-order current sources on the rhs of Eq. (A23) and will be neglected.

With the above considerations, the expression for  $\tilde{j}_p(\mathbf{v})$  reduces to

$$\tilde{j}_p(\mathbf{v}) = \tilde{j}_0^{(1)}(\mathbf{v}) + \tilde{j}_0^{(2)}(\mathbf{v}) + \tilde{j}_p^{(1)}(\mathbf{v}) - \Delta\tilde{M}_p(\mathbf{v})\tilde{p}(\mathbf{v}) \quad (\text{A28})$$

with

$$\Delta\tilde{M}_p(\mathbf{v}) = \frac{(2\pi)^2}{S_0} \int d\mathbf{k} \tilde{\xi}(\mathbf{v}-\mathbf{k}) \left[ \tilde{A}_1(\mathbf{v}, \mathbf{k}) \tilde{M}_p^{-1}(k) \tilde{\xi}(\mathbf{k}-\mathbf{v}) \tilde{A}_1(\mathbf{k}, \mathbf{v}) - \frac{\omega^2}{c^2} \frac{k_y^2}{k^2} \tilde{A}_4(k) \tilde{M}_s^{-1}(k) \tilde{\xi}(\mathbf{k}-\mathbf{v}) \tilde{A}_3(v) \right]. \quad (\text{A29})$$

We obtain the  $p$ -wave amplitudes to second order by inserting Eq. (A28) into Eq. (A1) which, after rearranging terms, yields

$$\tilde{p}(\mathbf{v}) = [\tilde{M}_p(v) + \Delta\tilde{M}_p(\mathbf{v})]^{-1} [\tilde{j}_0^{(1)}(\mathbf{v}) + \tilde{j}_p^{(1)}(\mathbf{v}) + \tilde{j}_0^{(2)}(\mathbf{v}) + \tilde{p}_0(\mathbf{k}_i^0) \delta(\mathbf{v}-\mathbf{k}_i^0)]. \quad (\text{A30})$$

For the specular direction we obtain the coordinate-space amplitudes by inverse Fourier transforming Eq. (A30) and letting  $\mathbf{v}=\mathbf{k}_i^0$ . In this case  $j_0^{(1)}(k_x^0)$  and  $j_p^{(1)}(k_x^0)=0$  since, as discussed previously, these involve  $\langle \xi_1 \rangle$  and  $\langle \xi_2 \rangle$  which were chosen to be zero. For the  $p$ -polarized magnetic field vector  $\tilde{P}(k_x^0) e^{-ik_x^0 x}(0, k_x^0, 0)$ , we have that

$$\tilde{P}(k_x^0) = \begin{pmatrix} P_1^-(k_x^0) \\ P_2^+(k_x^0) \\ P_2^-(k_x^0) \\ P_3^+(k_x^0) \end{pmatrix} = [\tilde{M}_p(k_x^0) + \Delta\tilde{M}_p(k_x^0)]^{-1} \left[ \frac{(2\pi)^2}{S_0} \tilde{j}_0^{(2)}(k_x^0) + \tilde{p}_0(k_x^0) \right]. \quad (\text{A31})$$

The reflection coefficient in the specular direction is  $|P_1^-(k_x^0)|^2$  and can be obtained from Eq. (A31). From Eq. (A31) we notice that the dispersion relation for SP's is satisfied by those values of  $k_x^0$  for which the magnitude of the determinant of  $[\tilde{M}_p(k_x^0) + \Delta\tilde{M}_p(k_x^0)]$  is a minimum. This condition differs from the smooth multilayer system dispersion relation due to the presence of  $\Delta\tilde{M}_p(k_x^0)$ .

## B. Diffuse reflection intensity

For  $\mathbf{v} \neq \mathbf{k}_i^0$ , the  $\delta$  function  $\delta(\mathbf{v}-\mathbf{k}_i^0)$  does not contribute to  $\tilde{p}(\mathbf{v})$ , hence

$$\tilde{p}(\mathbf{v}) = [\tilde{M}_p(v) + \Delta\tilde{M}_p(\mathbf{v})]^{-1} [\tilde{j}_0^{(1)}(\mathbf{v}) + \tilde{j}_p^{(1)}(\mathbf{v}) + \tilde{j}_0^{(2)}(\mathbf{v})]. \quad (\text{A32})$$

We are interested in using Eq. (A32) to calculate the diffuse scattered radiation in region III of Fig. 9. This occurs for wave vectors  $\mathbf{v}$  in the  $x$ - $y$  plane such that the  $z$  component in medium III,

$$v_3 = \left[ \frac{\omega^2}{c^2} \epsilon_3 - v^2 \right]^{1/2},$$

is real, which will be the case for  $v < \omega/c$  (for  $\epsilon_3=1$ ). Since, for these values of  $\mathbf{v}$ , the matrix  $\tilde{M}_p(v)$  is nonresonant, the correction  $\Delta\tilde{M}_p(\mathbf{v})$  in Eq. (A32) is not significant. Thus, an expression for diffuse scattered radiation calculated from Eq. (A32) will not incorporate the change in dispersion relation, Eq. (A31).

To include this effect, we use Eq. (A31) to correct the  $p$ -wave amplitudes which serve as inputs for the source  $\tilde{j}_p^{(1)}(\mathbf{v})$  in Eq. (A32). Thus, instead of using Eq. (A26) to obtain Eq. (A32) we use

$$\tilde{j}_p^{(1)}(\mathbf{v}) = -i\tilde{\xi}(\mathbf{v}-\mathbf{k}_i^0)\tilde{A}_1(\mathbf{v},\mathbf{k}_i^0)\tilde{P}(k_x^0), \quad (\text{A26}')$$

where  $\tilde{P}(k_x^0)$  is given by Eq. (A31). With this change, the scattered distribution will be larger when the modified dispersion relation is satisfied.

The scattered radiation in medium III, expressed as a differential intensity per solid angle normalized to the incident intensity, for the case in which the observation plane coincides with the incidence plane ( $p$ -polarized scattering), is<sup>22</sup>

$$\frac{1}{I_0} \frac{dI(\theta_s)}{d\Omega} = \frac{(2\pi)^2}{S_0} \frac{1}{n} \left[ \frac{2\pi}{\lambda} \right]^2 \frac{\cos^2\theta_s \sin^2\theta_s}{\cos\theta \sin^2\theta} |p_3^+(v_x)|^2, \quad (\text{A33})$$

where  $S_0$  is the illuminated area on the surface,  $\theta_s$  is the observation angle in the  $x$ - $z$  plane, and  $\theta$  is the incidence angle (see Fig. 8). It is assumed for Eq. (A33) that medium III is vacuum.

The elements of the matrix products defined previously in this section involve terms of the form  $|\hat{\xi}_i(\mathbf{k}-\mathbf{v})|^2$ , where  $i=1$  and  $2$  for each of the rough surfaces. In terms of the autocorrelation  $h_i(\rho)$  function for a surface, where

$$h_i(\rho) = \frac{1}{S_0} \int d\mathbf{r} \xi_i(\mathbf{r}+\rho)\xi_i(\mathbf{r})$$

and  $S_0$  = area of integration,

$$|\hat{\xi}_i(\mathbf{k})|^2 = \frac{S_0}{4\pi^2} \{h_i(\rho)\},$$

where  $\{ \}$  is the Fourier transform. We shall assume a Gaussian autocorrelation, as given by Eq. (3), which yields

$$|\hat{\xi}_i(\mathbf{k})|^2 = \frac{S_0}{16\pi^3} \delta_i^2 \sigma_i^2 \exp\left[-\frac{k^2 \sigma_i^2}{4}\right],$$

where  $\delta_i$  and  $\sigma_i$  are the rms height and correlation length for surface  $i$ , respectively.

Equation (A33) can be written in a more standard form if we neglect, in Eq. (A32), the higher-order corrections  $\Delta\tilde{M}_p(\mathbf{v})$  and  $\tilde{j}_0^{(2)}(\mathbf{v})$ . In this case, Eq. (A32) assumes the form

$$\tilde{p}(\mathbf{v}) = \tilde{M}_p^{-1}(v) [\tilde{j}_0^{(1)}(\mathbf{v}) + \tilde{j}_p^{(1)}(\mathbf{v})], \quad (\text{A32}')$$

and Eq. (33) becomes

$$\frac{1}{I_0} \frac{dI}{d\Omega}(\theta_s) = \frac{\pi^3 n}{(\cos\theta)\lambda^4} \left\{ \sum_{l=1}^2 f_l(\theta_s) \delta_l^2 \sigma_l^2 \exp\left[-\left(\frac{\pi}{\lambda}\right)^2 (\sin\theta_s - n \sin\theta)^2 \sigma_l^2\right] \right\}, \quad (\text{A34})$$

where

$$\begin{aligned} f_l(\theta_s) = & \left| \frac{1}{\eta_0 D(\theta_s)} \left\{ t_{21}(\theta_s, l) t_{32}(\theta_s) \cos\theta_s [(\epsilon_l - 1)E_{lx}(z_l) - (\epsilon_{l+1} - 1)E_{l+1,x}(z_l)] \right. \right. \\ & \left. \left. + t_{12}(\theta_s, l) t_{23}(\theta_s) \sin\theta_s \left[ (\epsilon_l - 1) \left(\frac{\epsilon_1}{\epsilon_l}\right)^{1/2} E_{lz}(z_l) - (\epsilon_{l+1} - 1) \left(\frac{\epsilon_1}{\epsilon_{l+1}}\right)^{1/2} E_{l+1,z}(z_l) \right] \right\} \right|^2 \\ & \times \exp\left[-\frac{4\pi}{\lambda} |\epsilon_2 - \sin^2\theta_s|^{1/2} (d - z_l)\right], \end{aligned} \quad (\text{A35})$$

$\eta_0$  is the free-space wave impedance, and  $E_{mx}(z_l)$ ,  $E_{mz}(z_l)$  are the  $x$  and  $z$  components of the electric field in medium  $m$ , for an incident magnetic field having unitary amplitude evaluated at the plane  $z=z_l$ , where  $z_{l=1}=0$  and  $z_{l=2}=d$ . The other terms in Eq. (A35) are given by

$$D(\theta_s) = 1 + r_{12}(\theta_s) r_{23}(\theta_s) \exp\left[-i\frac{4\pi}{\lambda} (\epsilon_2 - \sin^2\theta_s)^{1/2} d\right],$$

$$t_{ij}(\theta_s) = 1 + r_{ij}(\theta_s) \text{ for } i, j = 2, 3, i \neq j,$$

and

$$t_{ij}(\theta_s, l) = 1 + r_{ij}(\theta_s) \exp \left[ -i \frac{4\pi}{\lambda} (\varepsilon_2 - \sin^2 \theta_s)^{1/2} z_l \right],$$

for  $i, j = 1, 2$  and  $i \neq j$ . The  $r_{ij}$ 's are the single interface reflection coefficients for  $p$ -polarized waves. We write

$$r_{ij}(\theta_s) = \frac{\varepsilon_i (\varepsilon_j - \sin^2 \theta_s)^{1/2} - \varepsilon_j (\varepsilon_i - \sin^2 \theta_s)^{1/2}}{\varepsilon_i (\varepsilon_j - \sin^2 \theta_s)^{1/2} + \varepsilon_j (\varepsilon_i - \sin^2 \theta_s)^{1/2}},$$

$i, j = 1, 2, 3; i \neq j$ .

We note in Eq. (A34) that, for correlation lengths small compared to the wavelength, i.e.,  $(\sigma_l/\lambda) \ll 1$ ,  $l = 1, 2$ ,  $(1/I_0)(dI/d\Omega)$  varies as  $\lambda^{-4}$  in agreement with the Rayleigh scattering dependence.

In the small roughness limit, for which the roughness effect on the dispersion relation is negligible, the  $x$  components of  $E$  and  $H$  fields are approximately continuous across each interface. In this case, it can be shown that  $f_l(\theta_s)$  in Eq. (A35) reduces to the expression given by Kretschmann.<sup>33</sup>

### C. Modification of the plasmon dispersion relationship

To compare the results obtained in this section for the change in dispersion relation due to roughness with the results obtained previously within other approaches,<sup>25,26</sup> we will calculate this modification for the case of a single rough interface between two semi-infinite media, one of them (medium II) being a metal and the other (medium III), a vacuum. We can reduce our multilayer system of Fig. 8 to a single interface between media II and III by eliminating the first and second rows and columns of all matrices defined in this section and then making  $d = 0$  so that the new coordinate system has  $z = 0$  on the interface. The  $p$  wave amplitudes are obtained from  $\begin{pmatrix} p_2 \\ p_3 \end{pmatrix}$ . With these considerations, we find that

$$\Delta \tilde{M}_p(k_x^0) = \begin{pmatrix} \Delta M_{11}(k_x^0) & 0 \\ \Delta M_{21}(k_x^0) & 0 \end{pmatrix} \quad (\text{A36})$$

with

$$\Delta M_{11}(k_x^0) = \frac{(2\pi)^2}{S_0} \frac{(\varepsilon_2 - 1)^2}{\varepsilon_2} \int d\mathbf{k} |\hat{\xi}_2(\mathbf{k} - \mathbf{k}_l^0)|^2 \left[ \frac{1}{k_2 + k_3 \varepsilon_2} (k_2 k_2^0 k_3 k_x^2 / k^2 + k_x k_2 k_x^0) + \frac{\omega^2}{c^2} \frac{k_y^2 k_2^0}{k^2 (k_2 + k_3)} \right], \quad (\text{A37})$$

$$\Delta M_{21}(k_x^0) = \frac{(2\pi)^2}{S_0} \frac{(\varepsilon_2 - 1)^2}{\varepsilon_2} \int d\mathbf{k} |\hat{\xi}_2(\mathbf{k} - \mathbf{k}_l^0)|^2 \frac{1}{k_2 + k_3 \varepsilon_2} [k_3 k_2^0 k_x k_x^0 + k^2 (k_x^0)^2]. \quad (\text{A38})$$

The matrix  $\Delta \tilde{M}_p$  in Eq. (A36) modifies the location of the poles of  $\tilde{M}_p$ . The new poles which yield the modified dispersion relation are the roots of  $\det[\tilde{M}_p(k_x^0) + \Delta \tilde{M}_p(k_x^0)] = 0$ , which gives

$$\det \begin{pmatrix} 1 + \Delta M_{11}(k_x^0) & 1 \\ \frac{k_2^0}{\varepsilon_2} + \Delta M_{21}(k_x^0) & -k_3^0 \end{pmatrix} = 0. \quad (\text{A39})$$

From Eq. (A37) we have that

$$k_2^0 + k_3^0 \varepsilon_2 = -\varepsilon_2 [\Delta M_{21}(k_x^0) + k_3^0 \Delta M_{11}(k_x^0)]. \quad (\text{A40})$$

The solution for  $k_x^0$  from Eq. (A40) gives the dispersion relation for SP's including the roughness effect to second order. By substituting Eqs. (A37) and (A38) into (A40) one obtains, after a few manipulations,

$$k_3^0 \varepsilon_2 + k_2^0 = -\frac{(2\pi)^2}{S_0} (\varepsilon_2 - 1)^2 \int d\mathbf{k} |\hat{\xi}(\mathbf{k} - \mathbf{k}_l^0)|^2 \frac{1}{k_2 + k_3 \varepsilon_2} [(k k_x^0 + k_3^0 k_2 \cos \phi)(k k_x^0 + k_3^0 k_2^0 \cos \phi) + k_3^0 k_2^0 (k^2 + k_2 k_2) \sin^2 \phi], \quad (\text{A41})$$

where  $k_x = k \cos \phi$  and  $k_y = k \sin \phi$ . The result given by Eq. (A41) is equivalent to the one presented by Maradudin and Zierau<sup>25</sup> and also agrees with the expression of Toigo *et al.*<sup>26</sup> for the change in dispersion relation in the small roughness limit.

For computational purposes, the double integral in Eq. (A41) can be reduced to a single integral in  $k$  if one makes use of polar coordinates for the two-dimensional  $k$  space.<sup>25</sup> In addition, we assume that  $k_x^0 = \text{Re}(k_{\text{SP}}) + \Delta k_{\text{SP}}$  is the solution to Eq. (A41), where  $\Delta k_{\text{SP}}$  is a complex wave vector shift whose real part represents the modification in the dispersion

relation of SP's and the imaginary part is the increase in damping resulting from roughness. To second order in  $\xi$

$$\Delta k_{\text{SP}} = \frac{\delta^2 \sigma^2}{2} \frac{|\epsilon_r|^{1/2}}{(\epsilon_r + 1)^2} \exp\left[-\frac{k'_{\text{SP}}{}^2 \sigma^2}{4}\right] \times \int_0^\infty k dk \frac{(\alpha' - \epsilon \alpha'_0)}{(k + k_{\text{SP}})(k - k_{\text{SP}})} \exp(-k^2 \sigma^2 / 4) \left\{ \left[ k^2 \left[ (k'_{\text{SP}})^2 - \frac{\alpha_0 \alpha'}{2} \right] + \alpha_0 \alpha' \alpha'_0 \right] I_0(k k'_{\text{SP}} \sigma^2 / 2) - k k'_{\text{SP}} (\alpha_0 \alpha' + \alpha'_0 \alpha) I_1 \left[ \frac{k k'_{\text{SP}} \sigma^2}{2} \right] + \frac{1}{2} \alpha_0 \alpha k^2 I_2(k k'_{\text{SP}} \sigma^2 / 2) \right\}, \quad (\text{A42})$$

where  $\epsilon_2 \equiv \epsilon = \epsilon_r + i\epsilon_i$  and we assumed  $|\epsilon_r| \gg |\epsilon_i|$ . The meaning of the other terms in Eq. (A42) is the following:

$$k_{\text{SP}} \equiv k'_{\text{SP}} + i k''_{\text{SP}} = \frac{\omega}{c} \left[ \frac{\epsilon}{\epsilon + 1} \right]^{1/2}, \quad (\text{A43a})$$

$$\alpha_0 \equiv i k_3^0 = \left[ k'_{\text{SP}} - \frac{\omega^2}{c^2} \right]^{1/2}, \quad (\text{A43b})$$

$$\alpha \equiv i k_2^0 = \left[ k'_{\text{SP}} - \frac{\omega^2}{c^2} \epsilon \right]^{1/2}, \quad (\text{A43c})$$

$$\alpha'_0 \equiv i k_3 = \left[ k^2 - \frac{\omega^2}{c^2} \right]^{1/2}, \quad (\text{A43d})$$

$$\alpha' \equiv i k_2 = \left[ k^2 - \frac{\omega^2}{c^2} \epsilon \right]^{1/2}. \quad (\text{A43e})$$

The functions  $I_0$ ,  $I_1$ , and  $I_2$  on the rhs of Eq. (A42) are modified Bessel functions of zeroth, first, and second order, respectively, and given by

$$I_n(x) = (-1)^n \frac{1}{2\pi} \int_0^{2\pi} \cos(n\phi) e^{-x \cos\phi} d\phi. \quad (\text{A44})$$

\*On leave from the Departamento de Eletronica e Sistemas, Universidade Federal de Pernambuco, 50000-Recife, PE, Brasil.

<sup>1</sup>J. D. E. McIntyre, in *Optical Properties of Solids, New Developments*, edited by B. O. Seraphin (North-Holland, Amsterdam, 1975), Chap. 11.

<sup>2</sup>D. E. Aspnes, in *Optical Properties of Solids, New Developments*, edited by B. O. Seraphin (North-Holland, Amsterdam, 1975), Chap. 15.

<sup>3</sup>K. Vedam and Samuel S. So, *Surf. Sci.* **29**, 379 (1972); I. Ohlidal and F. Lukes, *Opt. Acta* **19**, 817 (1972); I. Ohlidal, F. Lukes, and K. Navratil, *Surf. Sci.* **45**, 91 (1974); J. R. Blanco, P. J. McMarr, and K. Vedam, *Appl. Opt.* **24**, 3773 (1985).

<sup>4</sup>A. Otto, in *Optical Properties of Solids, New Developments*, edited by B. O. Seraphin (North-Holland, Amsterdam, 1975), Chap. 13.

<sup>5</sup>D. N. Mirlin, in *Surface Polaritons*, edited by V. M. Agranovich and D. L. Mills (North-Holland, Amsterdam, 1982), Chap. 1.

<sup>6</sup>E. Kretschmann, *Z. Phys.* **241**, 313 (1971).

<sup>7</sup>I. Pockrand, J. D. Swalen, J. G. Gordon II, and M. R. Philippot, *Surf. Sci.* **74**, 237 (1977).

<sup>8</sup>I. Pockrand, *Surf. Sci.* **72**, 577 (1978).

<sup>9</sup>W. P. Chen and J. M. Chen, *J. Opt. Soc. Am.* **71**, 189 (1981).

<sup>10</sup>D. Hornauer, H. Kapitza, and H. Raether, *J. Phys. D* **1**, L100 (1974).

<sup>11</sup>A. J. Braundmeier, Jr. and E. T. Arakawa, *J. Phys. Chem. Solids* **35**, 517 (1974).

<sup>12</sup>D. L. Hornauer, *Opt. Commun.* **16**, 76 (1976).

<sup>13</sup>R. Orłowsky, P. Urner, and D. Hornauer, *Surf. Sci.* **82**, 69 (1979).

<sup>14</sup>M. T. Flanagan and R. H. Pantell, *Electron. Lett.* **20**, 968 (1984).

<sup>15</sup>S. Wright, A. D. de Oliveira, and M. G. F. Wilson, *Electron. Lett.* **15**, 510 (1979).

<sup>16</sup>H. J. Simon, D. E. Mitchell, and J. G. Watson, *Phys. Rev. Lett.* **33**, 1531 (1974).

<sup>17</sup>Y. J. Chen, W. P. Chen, and E. Burstein, *Phys. Rev. Lett.* **36**, 1207 (1976).

<sup>18</sup>S. O. Sari, D. K. Cohen, and K. D. Scherkoske, *Phys. Rev. B* **21**, 2162 (1980).

<sup>19</sup>H. Raether, *Surf. Sci.* **125**, 624 (1983); in *Surface Polaritons*, edited by V. M. Agranovich and D. L. Mills (North-Holland, Amsterdam, 1982), Chap. 9.

<sup>20</sup>H. E. Bennett, J. M. Bennett, E. J. Ashley, and R. J. Motyka, *Phys. Rev.* **165**, 755 (1968).

- <sup>21</sup>R. Bruns and H. Raether, *Z. Phys.* **237**, 98 (1970).
- <sup>22</sup>E. Kroger and E. Kretschmann, *Z. Phys.* **237**, 1 (1970).
- <sup>23</sup>E. A. Stern, *Phys. Rev. Lett.* **19**, 1321 (1967).
- <sup>24</sup>A. A. Maradudin and D. L. Mills, *Phys. Rev. B* **11**, 1392 (1975).
- <sup>25</sup>A. A. Maradudin and W. Zierau, *Phys. Rev. B* **14**, 484 (1976).
- <sup>26</sup>F. Toigo, A. Marvin, V. Celli, and N. R. Hill, *Phys. Rev. B* **15**, 5618 (1977).
- <sup>27</sup>Lord Rayleigh, *Philos. Mag.* **14**, 70 (1907).
- <sup>28</sup>U. Fano, *J. Opt. Soc. Am.* **31**, 213 (1941).
- <sup>29</sup>See for example A. A. Maradudin, in *Surface Polaritons* (North-Holland, Amsterdam, 1982), Chap. 10, pp. 470–471 and Eq. (4.41), p. 480.
- <sup>30</sup>J. M. Elson, *Phys. Rev. B* **30**, 5460 (1984).
- <sup>31</sup>A. Daude, A. Savary, and S. Robin, *J. Opt. Soc. Am.* **62**, 1 (1972).
- <sup>32</sup>H. Raether, in *Physics of Thin Films* (Academic, New York, 1977), Vol. 9, p. 145.
- <sup>33</sup>E. Kretschmann, *Opt. Commun.* **5**, 331 (1972).

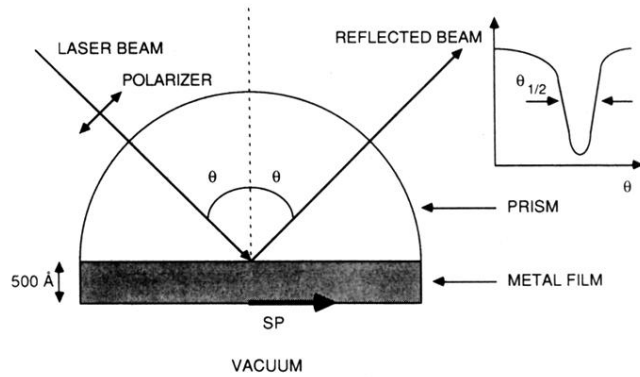


FIG. 1. Experimental configuration illustrating the excitation of a surface plasmon (SP) (Ref. 6). For incidence angles  $\theta$  above the total internal reflection value, an evanescent wave exists into the vacuum region. A resonant drop in the reflectivity is observed as the angle  $\theta$  is increased above this value. The minimum in the curve occurs when the phase velocity component of the incoming beam parallel to the prism-metal interface plane matches the SP phase velocity in the metal-vacuum interface.

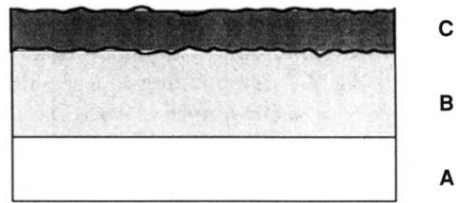


FIG. 2. Roughness simulation with use of underlayer. Region *A* is a glass substrate, region *B* is the underlayer ( $\text{CaF}_2$ ,  $\text{LiF}$ ,  $\text{MgF}_2$ , or  $\text{Ag}$ ) which produces the irregularities on the metal surface. The metal is designated as region *C*.

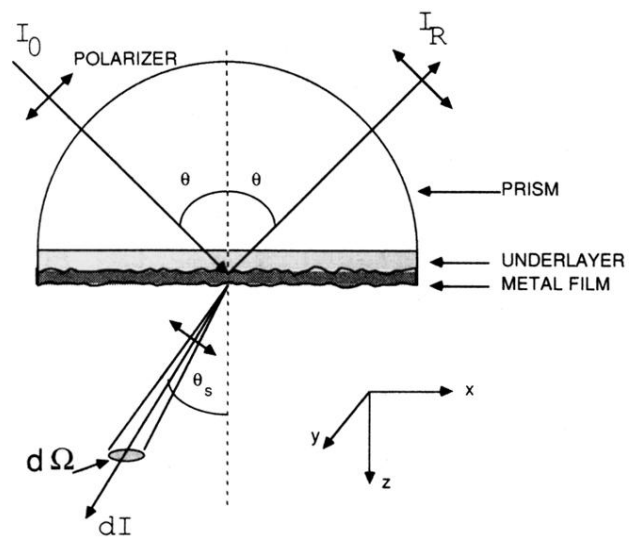


FIG. 3. Experimental arrangement for measuring specular and diffuse scattering intensities from thin metallic films.